J. Fluid Mech. (2007), *vol.* 585, *pp.* 421–456. © 2007 Cambridge University Press
doi:10.1017/S0022112007006775 Printed in the United Kingdom

Atomization of undulating liquid sheets

N. BREMOND, C. CLANET AND E. VILLERMAUX†

IRPHE, Université de Provence, Aix–Marseille 1, Technopôle de Château-Gombert, 49, rue Frédéric Joliot-Curie, 13384 Marseille Cedex 13, France

(Received 13 June 2006 and in revised form 27 March 2007)

The fragmentation of a laminar undulating liquid sheet flowing in quiescent air is investigated. Combining various observations and measurements we propose a sequential atomization scenario describing the overall sheet–drop transition in this configuration. The undulation results from a controlled primary Kelvin–Helmholtz instability. As the liquid travels through the undulating pattern, it experiences transient accelerations perpendicular to the sheet. These accelerations trigger a secondary instability responsible for the amplification of spanwise thickness modulations of the sheet. This mechanism, called the ‘wavy corridor’, is responsible for the sheet free edge indentations from which liquid ligaments emerge and break, forming drops. The final drop size distribution is of a Gamma type characterized by a unique parameter independent of the operating conditions once drop sizes are normalized by their mean.

1. Introduction

The transition from a compact liquid volume to a set of dispersed smaller drops – in the broad sense, the process of atomization – often involves as a transient stage the change of the liquid topology into a sheet shape. This transition is sometimes enforced by specific man-made devices, and also occurs spontaneously as a result of various impacts and blow-ups (Lefebvre 1989; Bayvel & Orzechowski 1993; Mason 1971). Then, the sheet is destabilized in some way to induce another transition towards the formation of threads or ligaments, the ultimate objects whose breakup (Savart 1833*a*; Plateau 1873; Rayleigh 1879; Eggers 1997) sets the size distribution of the final drops in the spray, depending on their state of corrugation while they fragment (Villermaux, Marmottant & Duplat 2004).

The purpose of this paper is to address the sheet–ligament–drop transition in the particular case when the sheet is *undulated*. This occurs naturally when its flowing velocity relative to the ambient medium is large enough (we will explain below how large this is) to amplify unstable waves via a shear, Kelvin–Helmholtz type of instability (Taylor 1960; Huang 1970; Lin 2003). Let us visualize how the atomization process is altered in that case: consider for instance the oblique impact of two identical liquid jets in quiescent air (Heidmann, Priem & Humphrey 1957; Bremond & Villermaux 2006). For low injection velocities, the resulting sheet takes a bay leaf shape bounded by a thicker rim. Ligaments are centrifuged from the rim and stretched as they break because of a longitudinal velocity gradient in the rim itself, which is a function of the impact angle and jet velocities. The final drop size distribution is thus found to be a function of the injection conditions. If now the jet speed is increased,

---

† Also at: Institut Universitaire de France.

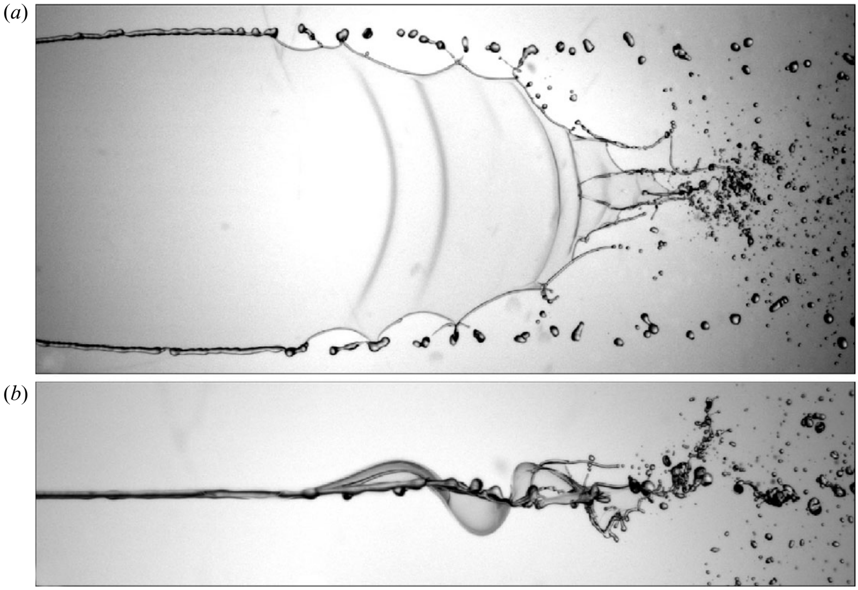

FIGURE 1. Front view (*a*) and side view (*b*) of the destabilization of a liquid sheet moving in air initially at rest.

the sheet starts to flap like a flag (figure 1). Large drops are still produced by the thick rim as described above, but now a finer spray appears at the centre of the end of the sheet where the unstable wave amplitude has developed. These smaller drops are produced through the destabilization of thinner ligaments normal to the sheet free edge. While the bigger drops formed through the destabilization of the thick rim around the sheet have a typical size set by the initial jet diameters, the average size of these smaller drops is now a strongly decreasing function of the jet velocities (Villermaux & Clanet 2002).

On the analytical side, a linear analysis of the shear instability of a fast moving sheet sandwiched between two infinite quiescent phases has been done by Squire (1953), York, Stubbs & Tek (1953) and Hagerty & Shea (1955). A review and an account of more recent developments can be found in Lin (2003). The instability sustains two discrete modes, varicose and sinuous, the growth rate of the latter being far larger than that of the former. Good agreement with experiments, both on the selected wavelength and associated growth rate, has been found by Asare, Takahashi & Hoffman (1981) for a sheet with a constant thickness and by Villermaux & Clanet (2002) for a radially expanding sheet.

The influence of the resulting wavy pattern on the sheet fragmentation process remains, on the contrary, conjectural. For instance, York *et al.* (1953) have proposed a rupture mechanism consisting of a series of lamellae parallel to the free rim and spaced by half the most unstable wavelength of the primary wavy pattern. The reason why the lamellae separate from each other is not given in this nevertheless commonly invoked scenario (Fraser *et al.* 1962; Dombrowski & Johns 1963). It is, however, incompatible with the experimental observation by the same authors showing that the sheet breaks via the formation of longitudinal ligaments, perpendicular to its mean free rim, similarly to what can be seen on figure 1. A mechanism producing fingers perpendicular to the free rim periodically accelerated by the incoming waves via a Rayleigh–Taylor-like instability (Rayleigh 1883; Taylor 1950) has been proposed by Villermaux & Clanet (2002). This scenario is encountered in different atomization configurations involving acceleration of the liquid/gas interface (Einsenklam 1964; James *et al.* 2003) and has been proved in some cases (Marmottant & Villermaux 2004*b*) to be the key effect responsible for the initiation of digitations at the interface, the precursor of the formation of ligaments.

These ligaments are common in various atomization processes and have been observed by Mansour & Chigier (1990) and Park *et al.* (2004) in the context of air-blasted liquid sheets. They were visible on the early drawings made by Savart (1833*c*) from sheets expanding radially from a jet. They also appear in the numerical simulations by Lozano, Garcia-Olivares & Dopazo (1998) and Kim & Sirignano (2000) when a spanwise perturbation is initially added to the flow.

However, and despite its widespread and natural occurrence, a global picture of the fragmentation of an undulating sheet offering a clear description of the relations between the consecutive instabilities is still lacking. As mentioned above, the source of the undulations is a shear, broadband instability. The experiments reported here were first conceived to control the amplitude, wavelength and frequency of the wave pattern, allowing a clear discussion of its impact on the fragmentation process and resulting atomization quality. The especially designed experimental set-up is depicted in § 2 as well as an overview of the experimental observations. Section 3 is devoted to the primary destabilization where the linear theory is compared to experiments. A discussion of the secondary instability is provided in § 4 and its consequences for the atomization scenario are examined in § 5. There, we propose a simple analysis which captures the essential physical processes involved in the sheet fragmentation, before we conclude. An Appendix analyses the fragmentation mechanism of a jet resulting from the merging of two jets.

2. Experiments and overview

2.1. *Formation of the liquid sheet*

Figure 2 depicts the formation of the liquid sheet and introduces the coordinates and parameters used. The sheet results from the normal impact of a round jet on a solid cylinder fitted with a thin jacket, a configuration inspired by Savart (1833*c*) and previously studied in various limits by Taylor (1959*a*, *b*, 1960), Huang (1970), Clanet & Villermaux (2002) and Villermaux & Clanet (2002). The jacket allows the ejection angle of the sheet with respect to the solid cylinder axis to be controlled at will, and was kept at a right angle in this study.

A gravity-driven stream of water provides a constant flow rate free of perturbations. The flow is directed through a flow meter, calibrated using a high-precision balance and a stopwatch, towards a cylindrical injector with a 21 mm inner diameter whose core contains a 30 mm long grid. The grid has a honeycomb shape containing about 15 hexagonal cells which break large perturbation structures. A round jet with a diameter d_j equal to 2.9 mm finally emerges from a 35 mm long converging nozzle for stabilizing the boundary layer. The injection protocol is such that the jet is as laminar as possible and with a thin boundary layer at the exit, i.e. with a close-to-uniform velocity profile. The mean jet velocity u_j deduced from the flow rate and jet diameter lies between 2.5 and $5\,\mathrm{m\,s^{-1}}$, leading to jet Weber numbers $We = \rho d_j u_j^2/\sigma$ smaller than 1000. Water surface tension and density are $\sigma = 0.073\,\mathrm{kg\,s^{-2}}$ and $\rho = 1000\,\mathrm{kg\,m^{-3}}$, respectively. The error in the mean jet velocity, incorporating flow fluctuations and accuracy of the measurements, is about $0.05\,\mathrm{m\,s^{-1}}$.

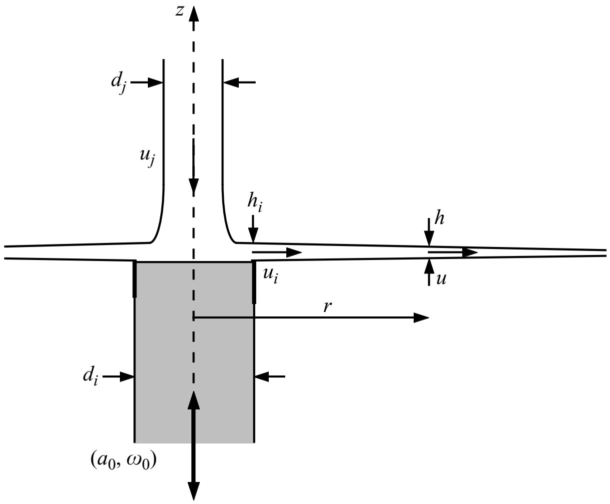

FIGURE 2. Formation of the axisymmetric liquid sheet.

FIGURE 3. Axisymmetric liquid sheet states: (*a*) Smooth regime. (*b*) Flapping regime for larger Weber number (higher than 1000). (*c*) Perturbation of the smooth regime by vertically oscillating the impact cylinder.

After the impact on a solid cylinder with a diameter $d_i = 6\,\mathrm{mm}$ and fitted with a thin jacket of the appropriate height, the liquid expands radially forming a flat disk. Without this thin jacket the liquid sheet takes a bell-like shape as discussed in Clanet & Villermaux (2002). An example is shown on figure 3(*a*) for a jet Weber number smaller than 1000. This situation is referred to as the smooth regime. If the jet velocity is increased, a shear instability develops at the liquid/air interface and the sheet flaps in a sinuous fashion like a flag, with a preferred wavelength superimposed on a noisy background as illustrated on figure 3(*b*).

Since our goal is to investigate the role played by such surface waves in the fragmentation process occurring at the edge of the sheet, the experiment has been designed to control the primary destabilization. The control is realized by oscillating the impact cylinder vertically with a vibrator (LDS-V406). It was possible in this way to independently tune the amplitude a_0 and the frequency f (pulsation $\omega_0 = 2\pi f$) of the oscillating motion of the impact point. This thus sets the oscillating motion of the train of fluid particles injected into the sheet from the impact location. A snapshot of the vibrated sheet is shown in figure 3(*c*) for a low Weber number corresponding to the smooth regime presented in figure 3(*a*). Amplitudes a_0, pulsations ω_0 and injection velocities u_j are always such that

$$\frac{a_0\omega_0}{u_j} \ll 1. \tag{2.1}$$

If $a_0\omega_0/u_j$ is close to 1, then the vertical oscillations of the impact cylinder will induce liquid velocity fluctuations in the sheet which will lead to kinematic packing of liquid since liquid particles flow at different speeds. This kind of behaviour is observed in liquid jets with a pulsating injection condition as reported by Meier, Klopper & Grabitz (1992), but it is unwanted here.

Let us recall the radial dependence of the sheet thickness $h(r)$ and flow velocity u. The mean velocity u_i on leaving the impact cylinder is reduced to βu_j due to viscous losses in the development of a boundary layer at the solid surface, and to the singular losses on crossing the jacket hump. The overall loss of momentum leads to a reduction of velocity by a factor $\beta \approx 0.97$ with an impact cylinder diameter d_i of 6 mm (Clanet & Villermaux 2002). If one assumes that the velocity profile has relaxed to a uniform profile as soon as the liquid is ejected from the impactor, mass and momentum conservation of the radial flow in the sheet imply that the velocity u is constant and equal to that of the fluid particles just after they have left the impactor, that is βu_j. Conservation of mass between the jet and a location r on the sheet gives

$$\frac{\pi}{4}\rho d_j^2 u_j = 2\pi\rho r h(r) u \tag{2.2}$$

yielding finally

$$u = \beta u_j, \tag{2.3}$$

$$h(r) = \frac{1}{\beta}\frac{d_j^2}{8r}. \tag{2.4}$$

The sheet thins with distance from the impactor, and the process is interrupted when capillary forces, proportional to $\sigma/h(r)$, become of the order of the incoming liquid inertia ρu^2. As measured by Bond (1935), Huang (1970) and many others, the radius R_0 of a radially expanding liquid sheet from the impact point to the location where the sheet breaks is, in the smooth regime,

$$\frac{R_0}{d_j} = \frac{We}{16}. \tag{2.5}$$

FIGURE 4. Vibrating liquid sheet as seen with the naked eye.

The Bond number $Bo = \sqrt{gR_0/u_j^2} = d_j/l_c$, where $l_c = \sqrt{\sigma/\rho g}$ is the capillary length and g is the acceleration due to gravity, is of the order of 0.2 so that gravity can be neglected.

2.2. *Experimental observations*

2.2.1. *Waves*

The first feature to be seen on the sheet when the impact cylinder is vibrating is shown in figure 4, taken with a long exposure time (20 ms) compared to the period of oscillations (6.7 ms). We note a circular, stationary (because of the long exposure time) interference pattern with wavelength decreasing towards the edge. If we now use a high-speed camera (Phantom V5.1) recording 4500 frames per second, corresponding to an exposure time of 0.22 ms, we observe the periodic formation of circular waves propagating towards the free edge of the sheet. A snapshot of the undulating sheet is shown on figure 5(*a*) showing the wavelength decreases as the waves reach the free edge. Interesting features are deduced from the spatio-temporal diagram constructed at the horizontal line marked on figure 5(*a*) shown on figure 5(*b*). We first note that the oscillation of the impact cylinder induces a periodic wavetrain with a constant frequency equal to the forcing frequency of the impactor f. The trajectory of the waves is measured from this space–time map by following the shadow at the waves crest. The velocity of the waves decreases as they approach the free edge. The liquid velocity being constant, the velocity difference between the flowing liquid and the waves is thus an increasing function of r. This behaviour is crucial for the sheet fragmentation process and will be discussed in § 4.

These observations allow a characterization of the propagating waves from a kinematic point of view, but information about their amplitude is lacking. We thus visualized the cross-section of the undulating sheet using a laser-induced fluorescence technique. Fluorescein is mixed with the water before it enters the injector. A laser sheet expanded from an Argon-ion laser working in mono-mode at 488 nm is oriented along a radius of the liquid sheet and perpendicular to its surface when it is flat.

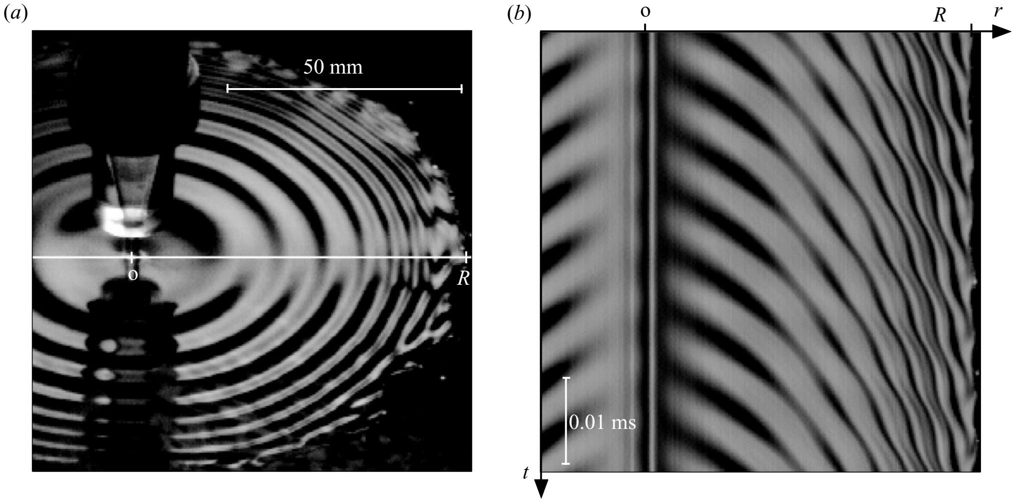

FIGURE 5. (*a*) Snapshot of an undulating liquid sheet. (*b*) Spatiotemporal diagram constructed at the horizontal line marked on (*a*).

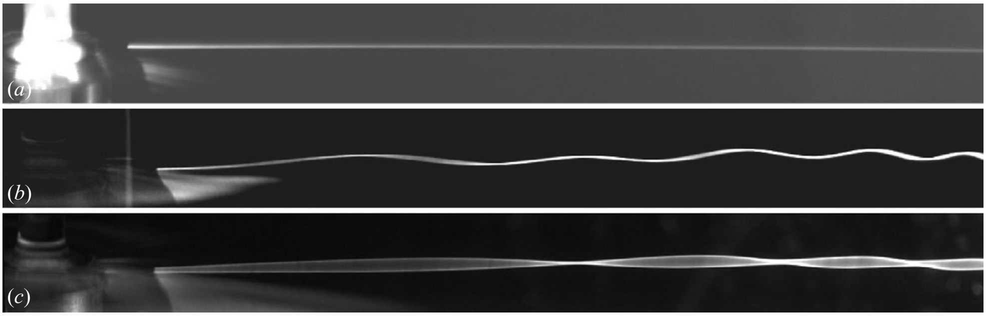

FIGURE 6. Radial cross-section of a water sheet with fluorescein revealed by a laser sheet, at rest (*a*), during oscillations of the impact rod for a short time exposure of the camera (*b*), and a longer one (*c*). $u_j = 3.5\ \mathrm{m\,s^{-1}}$, $f = 120\,\mathrm{Hz}$, $a_0 = 80\,\mu\mathrm{m}$.

Examples of such visualizations are displayed on figure 6. The first picture, (*a*), presents the initial state of the liquid sheet before it is perturbed by the vibration. The second snapshot, (*b*), reveals the forcing of sinusoidal waves with a decreasing wavelength as the wavetrain propagates to the sheet edge. Successive nodes and antinodes are observed if the exposure time of the camera is increased. The beat pattern is the sign of the interference of at least two wavetrains propagating with different velocities. This phenomenon is discussed in § 3.3.

Close-up views of the flapping sheet envelope are shown in figure 7 for several injection velocities u_j, the forcing $\{a_0, \omega_0\}$ being constant. The envelope contour is measured from binary pictures after applying an intensity threshold and subtracting the sheet thickness at each location obtained from figure 6(*a*). The corresponding amplitudes A_m of the first antinode normalized by the initial amplitude of the impact cylinder vibration a_0 are reported in figure 8 as a function of the jet velocity. We note that the ratio A_m/a_0 lies between 3 and 4 for jet velocities lower than $4\,\mathrm{m\,s^{-1}}$ and

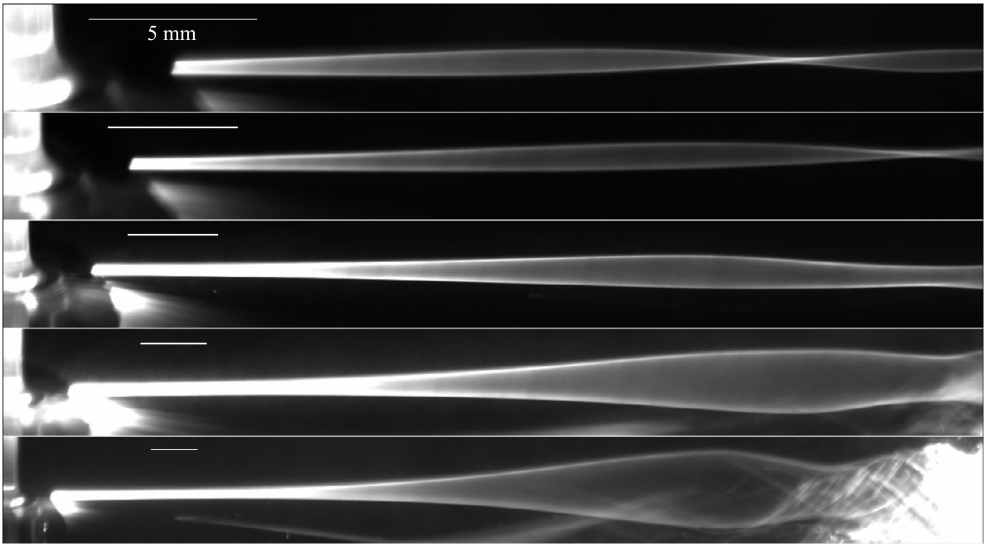

FIGURE 7. Envelopes of an undulating liquid sheet ($a_0 = 145\,\mu$m, $f = 120$ Hz) for several jet velocities, from top to bottom: 2.8, 3.5, 4.3, 5.0 and 5.6 m s^{-1}. The horizontal white line on each picture represents 5 mm, showing an amplification of the perturbation as the velocity increases.

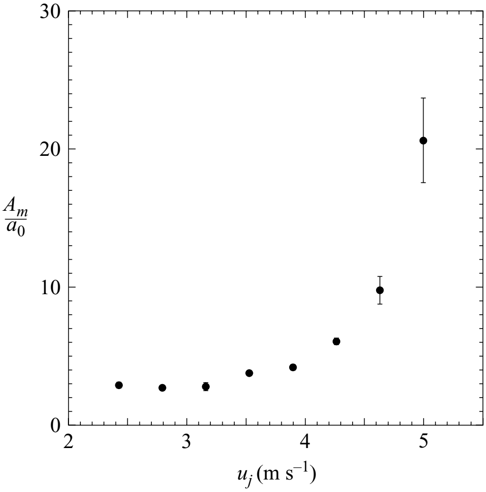

FIGURE 8. Amplitude of the first antinode A_m normalized by the forcing amplitude a_0 as a function of the jet velocity u_j for a frequency equal to 120 Hz.

then increases. This indicates an amplification of the initial perturbation and will be discussed in the analysis of the sheet destabilization in § 3.4.

2.2.2. *Fragmentation*

Starting with a smooth, steady sheet, and turning the impact cylinder oscillation on, the first moments of the sheet destabilization are shown on figure 9. The sheet is lit by an expanded laser beam and observed from the top. The interference pattern shown on the first picture before the forcing gives information on the sheet thickness field; each bright or dark fringe corresponds to a constant value of the thickness. For an

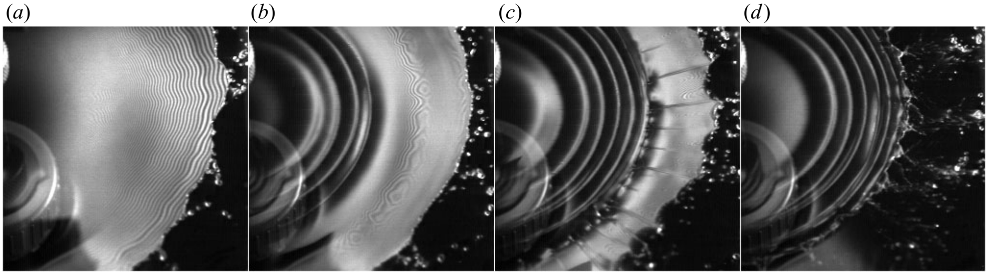

FIGURE 9. Initial instants of the sheet destabilization when the impact cylinder starts to oscillate. The sheet is lit by a laser revealing the initial thickness field on snapshot (*a*), some thickness modulations on (*b*) when waves propagate on the sheet, then longitudinal folds (*c*) and finally the retraction of the free edge (*d*). (*a*) $t = 0$, (*b*) 38 ms, (*c*) 55 ms, (*d*) 65 ms.

ideal case, the interference pattern would exhibit concentric circular fringes with an increasing distance between the fringes since the thickness decreases like $1/r$. A small deviation from this regular pattern is observed in figure 9(*a*) where the fringes present small oscillations indicating a weak, but visible, azimuthal modulation of the sheet thickness. The impact cylinder is then set into motion, triggering the formation of surface waves as shown in figure 9(*b*). The surface undulations make the visualization of the interference pattern difficult, but an enhancement of the azimuthal thickness modulation in front of the waves at a shorter length scale is nevertheless visible. The wavelength decreases as the wavetrain propagates and a catastrophic event occurs when it reaches a critical location: radial folds of the sheet appear in front of the wavetrain and the free rim moves rapidly backwards to its new equilibrium position (figure 9*c*). Since the location of the free rim depends on the local sheet thickness, this event is a sign of a thinning process induced by the surface undulations. This important, and in fact key phenomenon will be discussed in § 4.1.

The maximum radial extent of the liquid sheet is measured from an average of 20 snapshots taken from above and shown in figure 10. Without forcing (figure 10*a*), the sheet has a disk-like shape where drops are ejected, on average, uniformly around the rim. When undulations of the surface are imposed, the sheet shrinks (figure 10*b*), and this shrinkage is enhanced for higher frequencies of perturbation f (figure 10*c*) as well as for larger amplitude a_0 (figure 10*d*). When the sheet is vibrated, we note the presence of preferential sites of drop ejections on the rim. The number of these sites does not vary much with the forcing parameters and may be due to imperfections of the impact area since they move radially when the thin jacket around the impact cylinder is twisted.

The last step of the sheet fragmentation process is the formation of the drops. Two close-up views of the free rim without and with forcing are shown in figure 11. In both cases, the rim has cusps at the end of which ligaments emerge and break into drops via a capillary instability. This scenario is characteristic of sheet atomization when the liquid flow is initially perpendicular to the free rim, such as for the crown formed during splashes (Worthington 1908) or during the rupture of a soap film (Pandit & Davidson 1990). Despite this analogy, the cusp features differ from one case to another. First, the cusp signs of curvature are different. Second, as mentioned previously, the location of the cusps is nearly stationary when the sheet is vibrated while they move around the rim in a random fashion when the sheet is free of vibration. It will seen in § 4.1 that the surface undulations are responsible for the

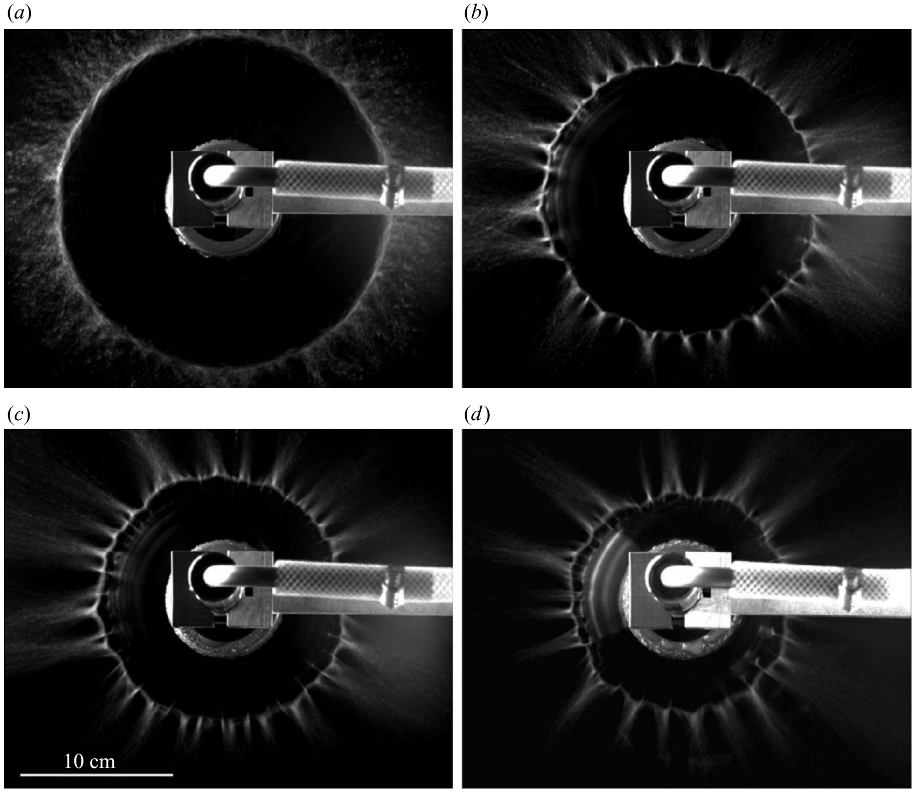

FIGURE 10. Global top views of a radially expanding liquid sheet ($We = 604$) for several forcing conditions: (*a*) free case, (*b*) $f = 120$ Hz, $a_0 = 0.10$ mm, (*c*) $f = 180$ Hz, $a_0 = 0.10$ mm and (*d*) $f = 180$ Hz, $a_0 = 0.16$ mm. The common length scale is indicated in (*c*).

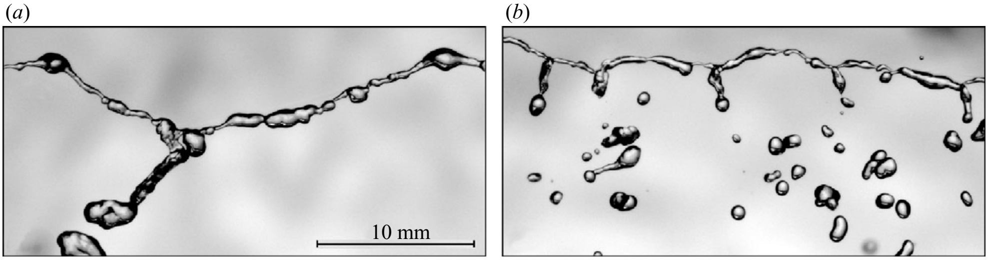

FIGURE 11. Close-up top views of the free rim without perturbations (*a*) and with a forcing at 120 Hz (*b*). The scale indicated in (*a*) is the same for both images.

amplification of azimuthal modulations of the sheet thickness, and therefore of the rim shape.

The drop size measurements have been taken from a collection of frozen images of the spray obtained by a back-lightning 5 µs flash lamp triggered by a Hamamatsu ORCA 1280 × 1024 pixels CCD array. An example is shown in figure 12(*a*). The image processing technique was originally described in Marmottant & Villermaux (2004*b*). The diameter d of the in-focus drops is determined from their projected area A by $d = (4A/\pi)^{1/2}$. Blurred, overlapping drops and those smaller than 40 pixels on the original images are rejected. Of the order of 1500 to 5000 drops were processed

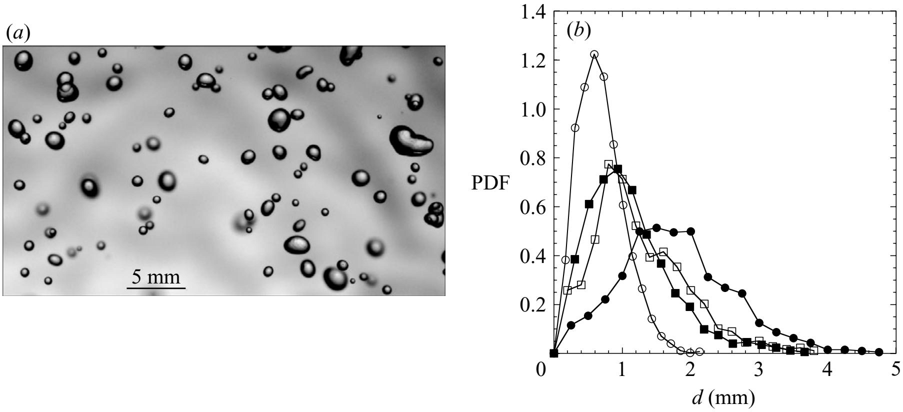

FIGURE 12. (*a*) Snapshot of the spray used for the drop size characterization. (*b*) Probability density functions of the drop diameter d for $We = 620$: ●, free case; ○, $a_0 = 0.05$ mm and $f = 200$ Hz; ■, $a_0 = 0.05$ mm and $f = 120$ Hz; □, $a_0 = 0.01$ mm and $f = 200$ Hz.

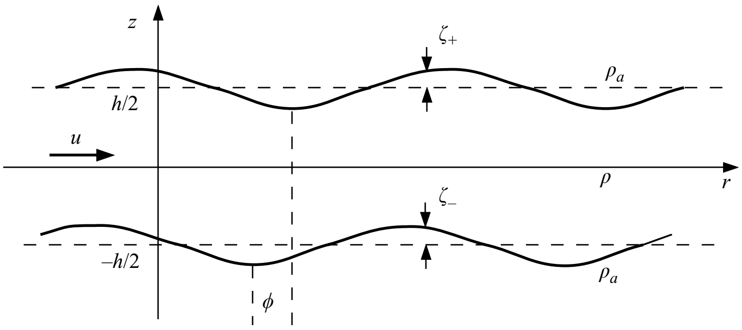

FIGURE 13. Sketch of the destabilization of a plane liquid sheet of thickness h in air at rest.

for each forcing condition. The resulting probability density function (p.d.f.) of the drop diameter d is reported in figure 12(*b*). The diameter distribution exhibits a peak around a millimetric size corresponding to the order of magnitude of the jet diameter d_j. The mean drop diameter is a decreasing function of the forcing parameters $\{a_0, f\}$.

3. Flapping instability

3.1. *Linear stability*

A thin liquid sheet of density ρ and thickness h moving with a uniform velocity u in air of density ρ_a initially at rest (figure 13) develops a Kelvin–Helmholtz-type instability (Helmholtz 1868; Kelvin 1871). A linear stability analysis of this peculiar configuration, namely two free surfaces, was originally done by Squire (1953), York *et al.* (1953) and Hagerty & Shea (1955) using normal modes (Chandrasekhar 1961; Drazin & Reid 1981) in the inviscid limit. The position of both free surfaces is perturbed by small amounts, such as $\zeta_+ = \zeta_0 \exp(\mathrm{i}kr - \mathrm{i}\omega t)$ for the upper interface and $\zeta_- = \zeta_0 \exp(\mathrm{i}kr - \mathrm{i}\omega t + \phi)$ for the lower one. This parallel flow (i.e. h independent of r) description is justified as long as

$$\frac{\lambda}{h}\frac{\mathrm{d}h}{\mathrm{d}r} \ll 1 \qquad (3.1)$$

where $\lambda = 2\pi/k$ is the undulation wavelength, a condition always fulfilled here: $(\mathrm{d}h/\mathrm{d}r)/h$ is indeed equal to $1/r$ since $h(r)$ is a power law of r, and λ quickly becomes much larger than r.

Two possible destabilization modes are found to coexist depending on the phase ϕ between the interfaces, a varicose mode ($\phi = \pi/2$) and a sinuous mode ($\phi = 0$). The dispersion relation for the sinuous mode which here is excited by the vertical oscillation of the impactor, is (e.g. Squire 1953)

$$\omega = \frac{uk\tanh(kh/2)}{\tanh(kh/2)+\alpha} \pm \frac{(\sigma k^3(\tanh(kh/2)+\alpha)/\rho - \alpha u^2k^2\tanh(kh/2))^{1/2}}{\tanh(kh/2)+\alpha} \tag{3.2}$$

where the density ratio ρ_a/ρ is denoted by α. We choose the jet diameter d_j and the jet velocity u_j, and hence the time d_j/u_j as characteristic scales. The dimensionless variables are marked with a tilde. For clarity, the friction factor $\beta \approx 0.97$ is set to one. From equations (2.3) and (2.4), the following transformation has thus to be done for all the subsequent equations when comparing with experiments:

$$\left\{\tilde{r} = \frac{r}{d_j},\ \tilde{\omega} = \omega\frac{d_j}{u_j},\ We\right\} \rightarrow \left\{\beta\tilde{r}, \tilde{\omega}/\beta, \beta^2 We\right\}. \tag{3.3}$$

The sinuous mode is the one naturally amplified (figure 1), and is also the one excited by the vibrating technique (figure 3*c*). The undulation wavelength is much larger than the sheet thickness. Using the definition of the sheet thickness h given by equation (2.4), the dimensionless dispersion relation of the sinuous mode in equation (3.2) is written, in the long-wave approximation $kh \ll 1$ as

$$\tilde{\omega} = \frac{\tilde{k}}{1+16\alpha\tilde{r}/\tilde{k}}\left(1 \pm \left(\frac{16\tilde{r}}{We}\left(1+\frac{16\alpha\tilde{r}}{\tilde{k}}\right) - \frac{16\alpha\tilde{r}}{\tilde{k}}\right)^{1/2}\right) \tag{3.4}$$

where $We = \rho d_j u_j^2/\sigma$ is the jet Weber number. Here we assume that the parallel flow description leading to equation (3.2) is locally valid: since the sheet thickness decreases as $1/r$, its tangent slope behaves as $1/r^2$ and becomes vanishingly small a few jet diameters away from the jet. The correction to the plane to the radial geometry (Weihs 1978) is a second-order effect (see Lin 2003 for instance). The system is unstable for wavenumbers such that the sign of the term under the square root of equation (3.4) is negative. Depending on the sign before this term, a perturbation will grow or decay exponentially with time. For a given radial location r on the sheet, the critical wavenumber $\tilde{k}_c$ below which the sheet becomes unstable is

$$\tilde{k}_c(\tilde{r}) = \alpha We\left(1 - \frac{16\tilde{r}}{We}\right). \tag{3.5}$$

The temporal growth rate, i.e. the imaginary part $\tilde{\omega}_i$ of $\tilde{\omega}$, is

$$\tilde{\omega}_i(\tilde{r},\tilde{k}) = \frac{\left(16\alpha\tilde{k}\tilde{r}\right)^{1/2}}{1+16\alpha\tilde{r}/\tilde{k}}\left(1 - \frac{16\tilde{r}}{We}\left(1+\frac{\tilde{k}}{16\alpha\tilde{r}}\right)\right)^{1/2}. \tag{3.6}$$

Since the growth rate is a function of the radial location $\tilde{r}$, the overall history of the amplification has to be integrated when the waves propagate towards the sheet edge. The perturbation analysis being made by a Fourier decomposition, the amplification has an exponential behaviour and a net gain $G(\tilde{r})$ can be thus defined by

$$G(\tilde{r}) = \ln\left(\frac{a(\tilde{\omega}_0,\tilde{r})}{a_0}\right) = \int_{\tilde{t}_i}^{\tilde{t}} \tilde{\omega}_i \mathrm{d}\tilde{t} = \int_{\tilde{r}_i}^{\tilde{r}} \tilde{\omega}_i \frac{\mathrm{d}\tilde{r}}{\tilde{c}_g}, \tag{3.7}$$

where $\tilde{c}_g$ is the unstable-wave group velocity given by

$$\tilde{c}_g = \frac{\partial \tilde{\omega}_r}{\partial \tilde{k}} = \frac{1 + 32\alpha \tilde{r}/\tilde{k}}{\left(1 + 16\alpha \tilde{r}/\tilde{k}\right)^2}, \tag{3.8}$$

$\tilde{\omega}_r$ being the real part of $\tilde{\omega}$. As shown by Villermaux & Clanet (2002), the most amplified wavenumber $\tilde{k}_m$ selected by the system is

$$\tilde{k}_m = \frac{\alpha We}{5}, \tag{3.9}$$

with a corresponding amplification factor, or gain, given by

$$G_m(\tilde{r}) = C\alpha We^{1/2}\tilde{r}^{3/2}, \tag{3.10}$$

where C is a constant of order unity, which will have to be adjusted using the measurements of the amplification.

This analysis can be used to anticipate how a most-amplified mode emerges from the ambient noise in the natural case. Let us now examine the case, like that in the present experimental situation, where the initial amplitude of a particular frequency is forced well above the noise.

3.2. *Onset of the instability*

We have shown in § 2.2 that the frequency f of the sinuous mode is the frequency of the impact cylinder oscillations, corrresponding to the dimensionless pulsation $\tilde{\omega}_0 = 2\pi f d_j/u_j$. This pulsation is equal to the real part of equation (3.4). The associated wavenumber is then

$$\tilde{k}(\tilde{r}) = \frac{\tilde{\omega}_0}{2}\left(1 + \left(1 + \frac{64\alpha\tilde{r}}{\tilde{\omega}_0}\right)^{1/2}\right). \tag{3.11}$$

Using equation (3.5) together with (3.11), the critical frequency $\tilde{\omega}_c$ below which the system is unstable is

$$\tilde{w}_c(\tilde{r}) = \alpha We\left(1 - \frac{16\tilde{r}}{We}\right)^2. \tag{3.12}$$

The sheet is then unstable until it reaches a critical radius r_c given by

$$\tilde{r}_c = \frac{We}{16}\left(1 - \left(\frac{\tilde{\omega}_0}{\alpha We}\right)^{1/2}\right) \tag{3.13}$$

The impact cylinder oscillations impose the frequency of the sinuous modes: an amplified one and a damped one. Those modes become stable beyond r_c and the waves should oscillate with a constant amplitude. Therefore, the sheet is completely stable for perturbation frequencies larger than a cutoff frequency ω_{co} for which the critical radius r_c is equal to the impact cylinder radius r_i. According to equation (3.12) the dimensionless cutoff frequency is

$$\tilde{w}_{co} = \alpha We\left(1 - \frac{16\tilde{r}_i}{We}\right)^2. \tag{3.14}$$

Examples of the envelope of the vibrating liquid sheet for frequencies larger than the cutoff frequency (3.14) are displayed in figure 14(a) for a Weber number equal to 850. The amplitude of the envelope is normalized by the forced amplitude a_0. We note that the size of the first antinode is constant as expected for this range of

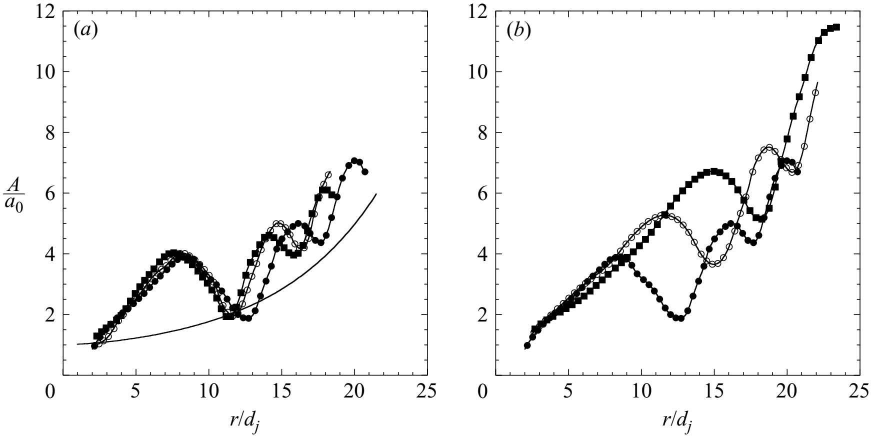

FIGURE 14. (*a*) Envelopes of a vibrating sheet for stable forcing frequencies (●, 220 Hz; ○, 240 Hz; ■, 260 Hz) and $We = 850$. The curve corresponds to the exponential of the maximum gain G_{max} of the naturally most amplified mode (3.10) with $C = 0.51$. (*b*) Envelope of a vibrating sheet for unstable forcing frequencies (■, 140 Hz; ○, 180 Hz; ●, 220 Hz) and $We = 850$.

frequencies, but the overall amplitude continues to increase as the waves propagate towards the free edge. The exponential increase of the naturally most-amplified mode k_m (3.9) with a corresponding gain G_m given by (3.10) for the same Weber number is also plotted on figure 14(*a*) with the constant C in equation (3.10) adjusted to

$$C = 0.5. \tag{3.15}$$

From this comparison, we conclude that even if the forcing falls on the stable branch of the instability, the most-amplified mode is still excited and leads to an amplification with r of the initial disturbance, as expected from a supercritical instability.

The envelopes for the same Weber number and lower frequencies are shown in figure 14(*b*). In this case, the amplification of the forced mode becomes more pronounced as the frequency decreases. The onset of the amplification of the forced mode is defined as when the amplitude of the first antinode starts to rise, as previously observed in figure 8. The frequencies corresponding to this onset are reported in figure 15 together with the predicted cutoff frequency given by equation (3.14). The excellent agreement shows the success of the linear theory in predicting the stability limits of this instability and its amplification properties even when the aspect ratio of the waves kA is of order unity.

3.3. *Stable forcing*

We now describe the wave dynamics in the regime for which the forcing frequency is larger than the cutoff frequency. In the long-wave approximation, $kh \ll 1$, with the approximation $\alpha = 0$ (i.e. neglecting the influence of the surrounding medium), the dispersion relation (3.2) becomes

$$\omega_0 = k\left(u \pm \sqrt{\frac{2\sigma}{\rho h}}\right) = k(u \pm c). \tag{3.16}$$

For this regime, the waves correspond to the non-dispersive waves studied by Taylor (1959*a*) where c is the intrinsic velocity of the stable sinuous wave. This velocity also corresponds to the retraction speed of the free edge of a liquid sheet with a thickness

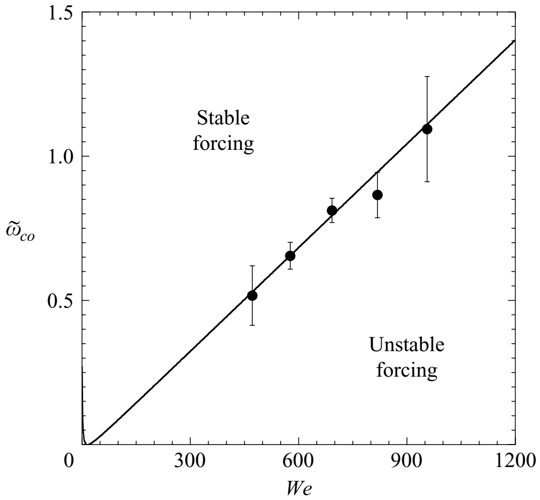

FIGURE 15. Experimental cutoff frequency (●) and that predicted by equation (3.14) (—) as a function of the jet Weber number We.

h due to capillary forces, as shown by Taylor (1959*b*) and Culick (1960). Because c is a decreasing function of h, which decreases with r, and the flow velocity u in the sheet is constant, there is a radial position R_0 where the liquid and the free-edge velocities are equal. The size of the expanding liquid sheet corresponds to R_0. Using the expression for the thickness, $h = d_j^2/8r$, the sheet radius R_0 is (Bond 1935) $R_0/d_j = We/16$.

The size of a liquid sheet is an increasing function of the jet velocity and diameter as first noticed by Savart (1833*b*). The intrinsic wave velocity c is therefore smaller than the liquid velocity u up to the free edge. From (3.16), two waves are generated, one denoted k_+ with a velocity $u + c$, and a second one denoted k_- with a velocity $u - c$. Because of their velocity difference, k_+ and k_- will interfere. This interference results in modulations of the mean envelope of the sheet surface, forming nodes and antinodes as shown on figure 6(*b*). The dimensionless velocity of the non-dispersive waves is

$$\tilde{V}_\pm = \frac{\tilde{\omega}_0}{\tilde{k}_\pm} = 1 \pm \tilde{c}. \tag{3.17}$$

Using the definitions of h and c, equation (3.17) becomes

$$\frac{\mathrm{d}\tilde{r}}{\mathrm{d}\tilde{t}} = 1 \pm \sqrt{\frac{r}{R_0}}. \tag{3.18}$$

The relationship between the radial position $\tilde{r}$ of a wave, located by its crest for example, and its lifetime $\tilde{t}$ is deduced from the integration of (3.18) from the impact cylinder edge $\tilde{r}_i$ to the radial location $\tilde{r}$. The relationships for the two waves are then

$$\tilde{t}_+ - \tilde{t}_i = 2R_0\left(\sqrt{\frac{r_+}{R_0}} - \ln\left(1 + \sqrt{\frac{r_+}{R_0}}\right) - \left(\sqrt{\frac{r_i}{R_0}} - \ln\left(1 + \sqrt{\frac{r_i}{R_0}}\right)\right)\right), \tag{3.19}$$

$$\tilde{t}_- - \tilde{t}_i = 2R_0\left(-\sqrt{\frac{r_-}{R_0}} - \ln\left(1 - \sqrt{\frac{r_-}{R_0}}\right) - \left(-\sqrt{\frac{r_i}{R_0}} - \ln\left(1 - \sqrt{\frac{r_i}{R_0}}\right)\right)\right), \tag{3.20}$$

where $\tilde{t}_i$ is the initial time of the wave formation at $\tilde{r} = \tilde{r}_i$. The experimental trajectory of a wave is measured from spatiotemporal diagrams such as the one

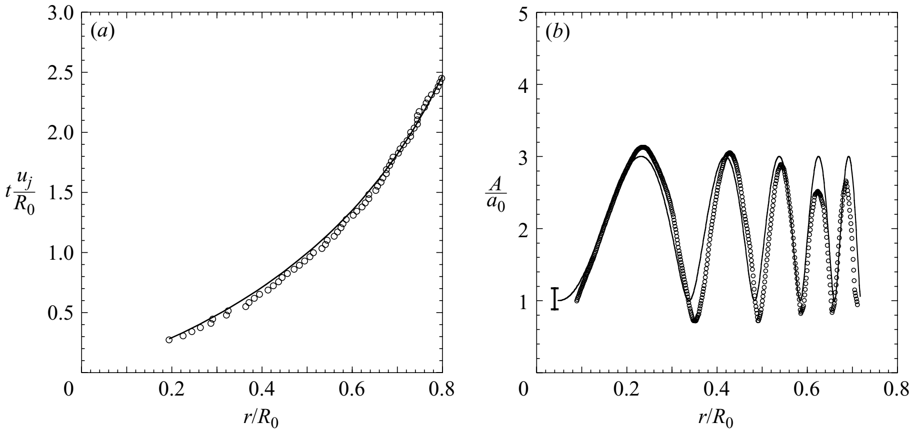

FIGURE 16. (*a*) Trajectory of a wave crest generated by a harmonic oscillation of the impact cylinder (○) ($u_j = 2.5$ m s^{-1}, $f = 100$ Hz). The curve represents the lifetime of the mode k_- given by equation (3.20). (*b*) Comparison of the experimental envelope of the oscillating sheet (○) ($u_j = 2.8$, $f = 150$ Hz) and that predicted by equation (3.22).

shown in figure 5(*b*). The wave slows down when it reaches the free edge, a direct result of the liquid sheet thinning; according to equation (3.17) the intrinsic wave velocity c is an increasing function of the position r. Therefore, this wave corresponds to the wave k_-. Figure 16(*a*) shows experimental trajectory of a wavetrain generated by oscillating the impact cylinder. The trajectory of the wave k_- predicted by equation (3.20) is also plotted and reproduces the experimental one well. The good agreement between experiment and theory is also a confirmation of the sheet velocity and thickness r-dependence given by equations (2.3) and (2.4).

The total deformation $a(\tilde{r},\tilde{t})$ of the interface, which corresponds to the distance between the sheet centreline and its initial position at $\tilde{y} = 0$, is the sum of the amplitudes of the two waves

$$a\left(\tilde{r},\tilde{t}\right) = a_1 \sin\left(\tilde{\omega}_0(\tilde{t}_-(\tilde{r}) - \tilde{t})\right) + a_2 \sin\left(\tilde{\omega}_0(\tilde{t}_+(\tilde{r}) - \tilde{t}) + \phi\right) \tag{3.21}$$

where ϕ is a phase shift between k_- and k_+ with respective amplitude a_1 and a_2. The two wavetrains will interfere because of their velocity difference. This interference results in a modulation of the average amplitude as observed on figure 6(*c*). The surface envelope A, deduced from the norm of a, is

$$A(\tilde{r}) = (a_1^2 + a_2^2 + 2a_1a_2\cos(\tilde{\omega}_0(\tilde{t}_+(\tilde{r}) - \tilde{t}_-(\tilde{r})) + \phi))^{1/2}. \tag{3.22}$$

The average amplitude described by equation (3.22) is plotted on figure 16(*b*) as well as the experimental one. Both envelopes are normalized by the initial amplitude a_0 of the impact cylinder. Two remarks arise from this comparison. First, in order to match the locations of the nodes and the antinodes, the phase shift ϕ is set to π. The waves are therefore out of phase. Second, the size of the antinodes is about three times the initial amplitude a_0, $A_m \sim 3a_0$. The initial displacement at $r = r_i$ of the free surface follows the motion of the impact rod, i.e. $a_1 - a_2 = a_0$. Therefore, from the surface envelope given by equation (3.22), $a_1 \sim 2a_0$ and $a_2 \sim a_0$ (and vice versa).

As discussed in § 3.2, the naturally most-amplified mode is still excited and is superimposed on the forced mode (figure 14*a*). The envelope given by equation (3.22) is thus valid for low jet Weber numbers for which the amplification factor (3.10) of the natural mode is weak, which is the case of the example reported on figure 14(*b*), corresponding to $We = 310$. It should consequently be noted that the kinematics of the waves described in this section for this type of forcing is relevant once the amplification of the wave height induced by the natural unstable mode for higher jet Weber numbers has been accounted for.

3.4. *Unstable forcing*

Let us now examine the regime for which the forcing is at a frequency falling in the unstable range. By oscillating the impact cylinder at a frequency $\tilde{\omega}_0$, we excite spatially developing modes with the same frequency $\tilde{\omega}_0$. The wavenumber $\tilde{k}$ is here a complex number whose imaginary part corresponds to the spatial growth rate of the instability. In the long-wave approximation, $\tilde{k}$ is the solution of the equation (Squire 1953)

$$\left(1-\frac{16\tilde{r}}{We}\right)\tilde{k}^3-2\tilde{\omega}_0\tilde{k}^2+\tilde{\omega}_0^2\tilde{k}+16\alpha\tilde{r}\tilde{\omega}_0^2=0. \tag{3.23}$$

A discussion of solutions of equation (3.23) is given in Lin (2003). The amplified mode is a complex wavenumber with a negative imaginary part $\tilde{k}_i$. The system is a spatially, convectively unstable developing flow and it has been shown by Villermaux & Clanet (2002) to be characterized well by adopting a translated temporal approach.

The convective nature of the instability is not *a priori* evident. Convective instabilities are those for which the disturbance sweep rate exceeds their instability growth rate ω_i. That rate scales as

$$\omega_i \sim \frac{u}{\lambda}\sqrt{\frac{\rho_a}{\rho}}\sqrt{\frac{\lambda}{h}} \tag{3.24}$$

for a wavelength λ (see Villermaux & Clanet 2002). The sweeping rate is of the order of u/λ so that

$$\omega_i\lambda/u = O\left(We_h^{-1/2}\right) \quad \text{where} \quad We_h=\frac{\rho u^2 h}{\sigma}. \tag{3.25}$$

But We_h is always larger than unity, up to the free sheet edge, so that convection is always dominant. We appreciate that this qualitative argument is not rigorous, but all the consequences that we draw from the convective hypothesis are consistent. This is why we have described the sheet destabilization by using the analysis presented in § 3.1, with a view to offering analytical solutions.

In the temporal description, the imposed frequency sets the real part of $\tilde{\omega}$ given by equation (3.4), and the corresponding wavenumber (3.11) associated with the gain G in equation (3.7). The gain increases with $\tilde{r}$ and reaches a constant beyond the critical radius $\tilde{r}_c$ where the forcing mode becomes stable. A maximal gain G_m is thus defined as

$$G_m=\int_{\tilde{r}_i}^{\tilde{r}_c}\tilde{\omega}_i\frac{\mathrm{d}\tilde{r}}{\tilde{c}_g}. \tag{3.26}$$

We describe the deflection amplitude of the sheet for a forcing such that the amplification is larger than that of the natural unstable mode. We therefore consider the two excited modes only, an amplified one corresponding to the positive solution of equation (3.4) and a damped one corresponding to the second solution. For $\tilde{r} < \tilde{r}_c$, the total deflection a of the sheet surface is the sum of the two:

$$a\left(\tilde{r},\tilde{t}\right)=\left(a_1\mathrm{e}^{G(\tilde{r})}+a_2\mathrm{e}^{-G(\tilde{r})}\right)\sin\tilde{\omega}_0\tilde{t}, \tag{3.27}$$

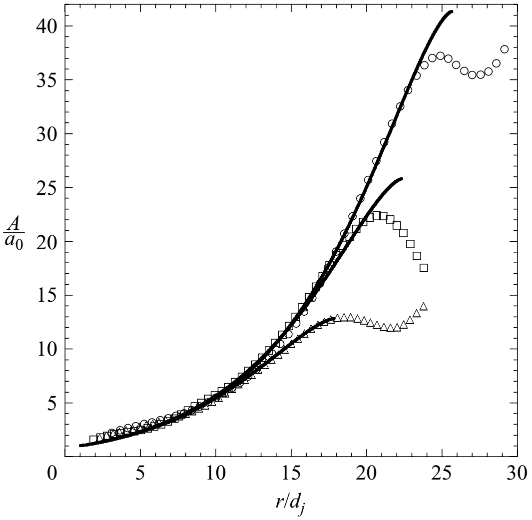

FIGURE 17. Comparison between the envelope predicted by equation (3.28) (continuous line) and the experimental one for three forcing frequencies: ○, 100 Hz; □, 120 Hz; △, 150 Hz. The Weber number is constant and equal to 990.

where a_1 and a_2 are the initial amplitudes of the two waves. The deflection a is initially equal to the forced amplitude a_0 at the impact cylinder, i.e. $a_2 = a_0 - a_1$. The surface envelope A normalized by a_0 is thus equal to

$$\frac{A(\tilde{r})}{a_0} = \frac{a_1}{a_0} \mathrm{e}^{G(\tilde{r})} + \left(1 - \frac{a_1}{a_0}\right) \mathrm{e}^{-G(\tilde{r})}. \tag{3.28}$$

According to the observations in the stable forcing, a_1/a_0 is around 2. Equation (3.28) is compared with experimental envelopes in figure 17 for $We = 990$ and several forcing frequencies. The evolution with $\tilde{r}$ is described well although a saturation is observed before the maximum amplitude A_m is reached.

When $\tilde{r} > \tilde{r}_c$, each mode becomes an oscillating wave with a constant amplitude defined by the value of the gain G at $\tilde{r} = \tilde{r}_c$. As for the stable forcing described in § 3.3, the waves interfere and the maximum deflection A_m is given by the sum of the absolute amplitude of the two modes for $G(\tilde{r}_c) = G_m$:

$$\frac{A_m}{a_0} = \frac{a_1}{a_0} \mathrm{e}^{G_m} + \left(\frac{a_1}{a_0} - 1\right) \mathrm{e}^{-G_m}. \tag{3.29}$$

The maximum deflection A_m normalized by the initial amplitude a_0 of the disturbance is compared in figure 18 with the measurements of the size of the first antinode. A relatively good agreement is found except close to the resonance of the instability where the experimental amplification is a little lower than predicted. The maximum deflection is measured for several initial amplitudes a_0 of the perturbation leading to an increase of the error bar for high amplification, i.e. for large jet Weber numbers. The maximum amplification decreases when the initial amplitude is too large indicating a saturation of the instability growth.

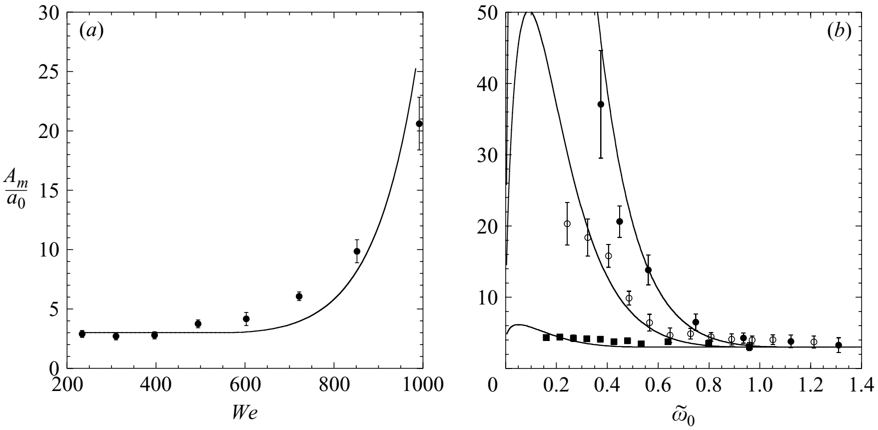

FIGURE 18. (*a*) Maximum amplification as a function of the Weber number for a forcing frequency set to 120 Hz. (*b*) Maximum amplification A_m measured at the first antinode as a function of the dimensionless pulsation $\tilde{\omega}_0$ for several Weber numbers: ●, 990; ○, 850; ■, 490. In both figures, the continuous line is given by equation (3.26).

4. Transverse indentations

The fragmentation of the sheet proceeds via a two-stage mechanism, the first of which has been analysed in the previous section. A secondary instability of a different nature then comes into play which is responsible for the sheet indentations, the formation of ligaments, and drops.

4.1. *Mechanism*

A peculiar feature of this flapping instability is that the surface waves it sustains propagate with a different speed than the liquid flow itself. This velocity difference becomes more pronounced as the waves approach the sheet edge. In its reference frame, a liquid particle propagates in a kind of 'wavy corridor' in which it is periodically accelerated upwards, and downwards. Therefore, and because of this difference, the sheet is subjected to an acceleration γ perpendicular to its plane whose intensity and direction depends on its curvature. The density interface between the water and the air is thus potentially unstable as has been known since Rayleigh (1883) and Taylor (1950). A complication arises from the fact that the two interfaces at the top and bottom of the sheet are close to each other: in addition to the standard capillary length constructed from the inertia of the liquid and capillary restoring forces i.e. $\ell \sim \sqrt{\sigma/\rho\gamma}$, a new length scale, namely the sheet thickness h comes into play. This situation has been investigated by Bremond & Villermaux (2005) who showed that the proximity of the interfaces (when $h/\ell < 1$) induces a considerable slowing down of the standard Rayleigh–Taylor instability. Its growth rate goes to zero as $h/\ell \rightarrow 0$. Using a strong, impulsive acceleration, the system can nevertheless be destabilized, and does so via growing thickness modulations. These modulations grow until their amplitude becomes of the order of the liquid film thickness, and the film perforates. Both the sheet perforation time and distance between the perforation locations are represented well by linear theory.

The sheet thickness and undulation-induced accelerations are such in the present problem that perforations are not observed (see figure 19). However, the thickness field modulations induced by this instability play a decisive role in the sheet breakup.

FIGURE 19. Thickness field revealed through laser interference of (*a*) a smooth and free liquid sheet exhibiting smooth azimuthal thickness modulations, and (*b*) with forced surface undulations where the transverse modulations of the thickness are amplified. Both pictures cover the same field.

Consider a two-dimensional liquid sheet of thickness h subjected to an acceleration γ initially normal to its surface, lying along the x-axis. The density of the gas phase surrounding the sheet is neglected as well as the viscosity of the liquid. Perturbations of the interface position are expanded in Fourier modes $\exp(\mathrm{i}kx - \mathrm{i}\omega t)$ and the dispersion relation is written, following Keller & Kolodner (1954),

$$\omega^2 = \frac{\sigma k^3}{\rho}\coth(kh)\left\{1 \pm \left[1 - \left(1 - \left(\frac{k_c}{k}\right)^4\right)\tanh^2(kh)\right]^{1/2}\right\}, \tag{4.1}$$

where $k_c = \sqrt{\rho\gamma/\sigma} \sim \ell^{-1}$ is the capillary wavenumber based on the acceleration γ. Equation (4.1) with the minus sign has an unstable range of wavenumbers for $0 < k < k_c$. The dispersion curve is reproduced in figure 20 for $k_c h \gg 1$ and for $k_c h \ll 1$. On the unstable branch and for $k_c h \ll 1$, a condition always satisfied in the present case, the most-amplified wavenumber k_t of the secondary instability is (Bremond & Villermaux 2005)

$$k_t = \frac{1}{6^{1/6}} k_c^{4/3} h^{1/3}, \tag{4.2}$$

lying between 0 and k_c on a broad plateau of wavenumbers whose associated growth rate is close to the maximal growth rate

$$\omega_t = \left(\frac{\rho h \gamma^2}{2\sigma}\right)^{1/2}. \tag{4.3}$$

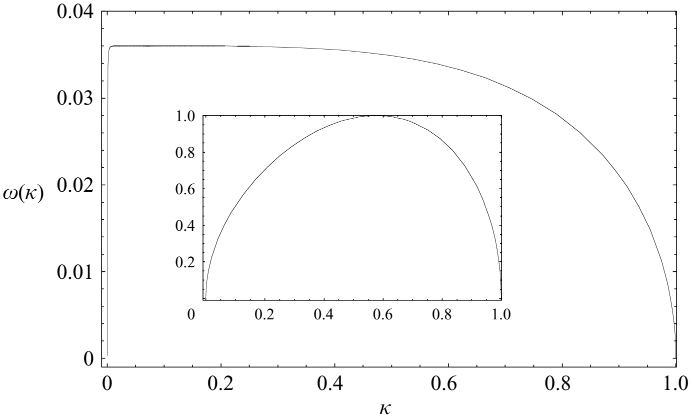

FIGURE 20. Imaginary part of the dispersion relation (4.1) where ω has been made dimensionless by $\sqrt{2/3\sqrt{3}\sqrt{\rho\gamma^3/\sigma}}$, the maximal growth rate of the infinite-thickness limit obtained when $k_c h \gg 1$, as a function of $\kappa = k/k_c$ with $k_c = \sqrt{\rho\gamma/\sigma}$ the capillary wavenumber. The curve has been drawn for $k_c h = 0.001$ and the inset shows the corresponding curve for $k_c h \gg 1$. Note the invariance of k_c with h, and the strong dependence of both the shape and amplitude of $\omega(\kappa)$ as h decreases. In particular, $\omega(\kappa)$ presents a plateau with uniform amplification irrespective of κ.

The acceleration experienced by a fluid particle travelling through the undulations is itself periodic in direction and intensity. Its maximal value is reached when the particle reaches an extremum of the primary wavy pattern, where the curvature is maximum. A rapid estimate is as follows: let Δu be the velocity contrast between the celerity $c = u_j - \Delta u$ of the propagating wave crests and the velocity of the radial flow u_j. The order of magnitude of the centrifugal acceleration is $\gamma \sim (\Delta u)^2/\mathscr{R}$ where $\mathscr{R}$ is the maximal wave curvature. If λ is the wavelength and a its amplitude, then $\mathscr{R}^{-1} \sim a/\lambda^2$. The transit time of a fluid particle over one wavelength is $T \sim \lambda/\Delta u$ so that $\gamma \sim a/T^2$. Since the frequency ω_0 at which the waves are released on the sheet is conserved along their path towards the free edge, $\omega_0 = (u_j - \Delta u)/\lambda$ is constant and therefore $\gamma = a\omega_0^2/(u_j/\Delta u - 1)^2$. This acceleration depends on the radial location r because of a possible dependence of a on r, and most important, because of the radial dependence of $\Delta u = \sqrt{2\sigma/\rho h(r)}$ with $h(r) \sim d_i^2/r$. In particular, it is expected to diverge at the smooth sheet edge where $\Delta u = u_j$. But the centrifugal Rayleigh–Taylor instability does not allow the waves to travel that far. The ingredients of the sheet atomization mechanism are depicted in figure 21.

The Rayleigh–Taylor instability of a thin sheet, such as the one seen on figure 19, thus does not select a particular wavenumber. There is a broad plateau of wavenumbers all with the same growth rate, so that the instability time scale is well-defined and allows us to predict correctly the sheet size in §4.2, but with no intrinsically selected wavenumber. That instability is therefore sensitive to the spatial structure of the injected noize, which is ultimately amplified, thus revealing the initial imperfection of the injection devices (injector + impact cylinder + jacket). The mode selection is thus intrinsic to the roughness of the injecting device, and does not come from a dimensional combination of physical parameters.

4.2. *Sheet radius*

A precise expression for γ can be derived from the discussion of the wave kinematics in the case $\omega_0 > \omega_{co}$ in §3.3. As just recalled, from the dispersion relation (3.16) and

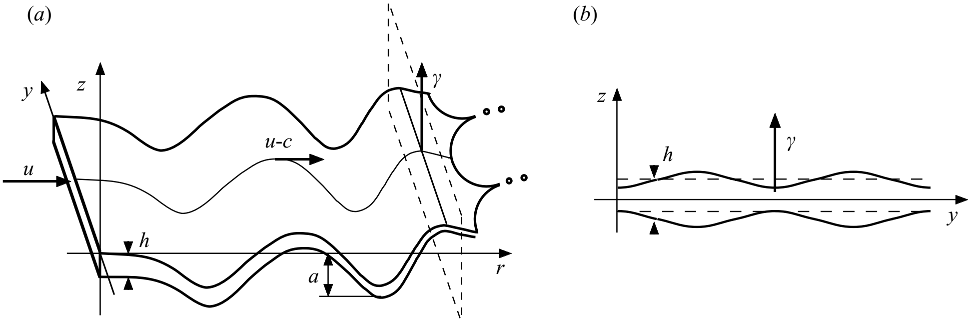

FIGURE 21. (*a*) Sketch of the 'wavy corridor' scenario: Since surface waves propagate with a different velocity ($u-c$) than the liquid (u), fluid particles are subjected to a centrifugal acceleration γ perpendicular to the sheet surface. That acceleration triggers a centrifugal instability responsible for the amplification of transverse thickness modulations which lead to the formation of ligaments perpendicular to the sheet edge. (*b*) Transverse cross-section of the liquid sheet showing the amplification of thickness modulations. The ligaments emerge from thicker regions.

according to sheet thinning (2.4), the wavenumber of k_- diverges to infinity as the waves approach the free edge since the wave intrinsic velocity c there is equal to the sheet velocity u (figure 5*a*). Therefore, the maximal acceleration γ induced by the mode k_- is

$$\gamma = \frac{\partial^2 a}{\partial t^2} = u^2\frac{\partial^2 a}{\partial r^2} = a_1\omega_0^2\frac{r}{R_0}\left(1-\left(\frac{r}{R_0}\right)^{1/2}\right)^{-2} \tag{4.4}$$

where R_0 is the size of the undisturbed liquid sheet and a_1 is the absolute amplitude of the wave k_-. Using the acceleration given by equation (4.4) and the sheet thickness in equation (2.4) with $\beta = 1$, the maximal growth rate in equation (4.3) of this secondary, centrifugal destabilization is finally

$$\omega_t = \frac{a_1\omega_0^2}{u_j}\frac{(r/R_0)^{1/2}}{\left(1-(r/R_0)^{1/2}\right)^2}. \tag{4.5}$$

The development of this instability will induce thickness modulations of the sheet. They will occur everywhere on its surface, and in particular in the azimuthal direction (figure 21). It is believed that they are responsible for the fast retraction and indentations of the free edge as observed in figure 9. But these azimuthal thickness modulations are likely to be amplified if the instability development has time to take place. In particular, the residence time T of the fluid particles in the vicinity of a wave crest, where the rate of amplification of the centrifugal instability ω_t is given, has to be large enough for an appreciable amplification to occur. We postulate (as in Villermaux & Clanet (2002) who were, however, working with a different component of the acceleration) that the transverse modulations will grow substantially when T is of the order of the characteristic instability time scale ω_t^{-1}, that is

$$T = \omega_t^{-1}, \tag{4.6}$$

which thus defines the radial location at which the sheet will fragment.

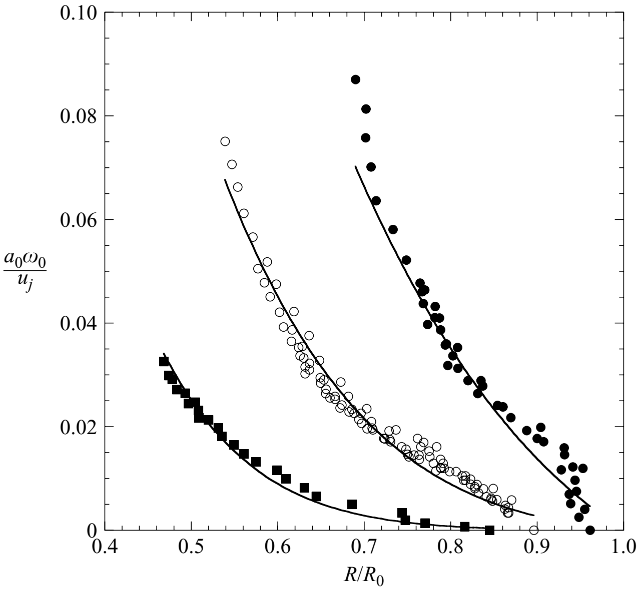

FIGURE 22. Correlation between the forcing and the sheet size for three Weber numbers: ●, 400; ○, 600; ■, 850. The continuous lines represent equation (4.9) by adjusting the constant K to 1 (consistently with equation (4.7)), in all cases.

The residence time T is defined from the wave frequency plus a Doppler shift in the particle reference frame as $\omega_0' = k\_u - \omega_0$ and is written

$$T = \frac{K}{\omega_0'} = \frac{K}{\omega_0}\frac{1-(r/R_0)^{1/2}}{(r/R_0)^{1/2}}, \tag{4.7}$$

where K is a constant of order unity to be determined from comparison with the experiments.

The acceleration γ is proportional to the total wave amplitude a_1. That amplitude is the imposed amplitude a_0, superimposed on the amplitude of the unstable noisy background, amplified according to the maximal gain obtained in § 3.3. We thus add the two contribution to give

$$a_1 = a_0 \exp\left(C\alpha We^{1/2}\tilde{r}^{3/2}\right). \tag{4.8}$$

The size R of the liquid sheet can now be computed from the fundamental criterion in equation (4.6). Using equations (4.5), (4.7) and (4.8), a relationship between the forcing $\{a_0, \omega_0\}$ and the normalized sheet size R/R_0 follows as

$$\frac{a_0\omega_0}{u_j} = \frac{1-(R/R_0)^{1/2}}{K\exp\left(C16^{-3/2}\alpha We^2(R/R_0)^{3/2}\right)}. \tag{4.9}$$

The dimensionless ratio $a_0\omega_0/u_j$ of the forcing is plotted versus the measured corresponding sheet size R normalized by R_0 in figure 22 for three jet Weber numbers and different amplitudes a_0 and frequencies ω_0. For each case, all the data collapse onto one master curve. The influence of the forcing $\{a_0, \omega_0\}$ on the sheet size becomes more important as We increases. This is a result of a larger amplification of the initial amplitude a_0 through the naturally most unstable mode at higher injection velocities. This amplification leads to stronger accelerations γ imposed on the sheet and therefore to larger growth rates ω_t of the secondary instability. This effect is included in equation (4.9) which, as shown in figure 22, predicts fairly well the experimental behaviour if the constant K is adjusted to the value 1.

The radial extent of an undulated liquid sheet thus results from the combination of two intricate instabilities whose linear analysis provides the relevant time and length scales to predict the overall behaviour.

5. Drop size distribution

Drops come from the breakup of roughly columnar objects, ligaments, whose topology is the only one to be made unstable by capillarity. Ligaments emerge, in the mean, normal to the free rim of the sheet (figures 11 and 21). They are formed at the tip of cusps bordering the sheet indentations through the merging of the corrugated cylinders constituting of the sheet rim. This scenario is general and holds for both cases, i.e. with and without forcing.

Villermaux *et al.* (2004) have discussed the general rules of the ligaments dynamics and have shown their decisive importance in understanding the size polydispersity of the resulting spray. The drop size distribution $P(d)$ associated with ligament breakup is a Gamma distribution

$$p(X) = \frac{n^n}{\Gamma(n)} X^{n-1} \mathrm{e}^{-nX} \quad \text{where} \quad X = \frac{d}{\langle d \rangle} \tag{5.1}$$

and $\langle d \rangle$ denotes the average drop size. The parameter n reflects the regularity of the initial shape of the ligament, i.e. its relative roughness which is the amplitude of its corrugations relative to its average diameter. A smooth thread has a very large n giving rise to a close to uniform distribution of drop sizes since $P(X) \overset{n\rightarrow\infty}{\longrightarrow} \delta(X-1)$, whereas a corrugated ligament with n finite induces a skewed, broader distribution of sizes with an exponential tail. Marmottant & Villermaux (2004*b*) and Bremond & Villermaux (2006) have shown how the value of n can be manipulated in an given experimental set-up by varying the parameters influencing the way the ligaments are produced.

The experimental probability density functions (p.d.f.) of the drop size d are displayed in figure 23 for a wide range of forcing and injection conditions: a_0 varies from 0 (no forcing) to 0.34 mm, f is between 80 Hz and 340 Hz and u_j ranges from 2.5 m s^{-1} to 5 m s^{-1}. When normalized by their mean $\langle d \rangle$, drops sizes are distributed in a unique way, a phenomenon already observed by Simmons (1977*a*, *b*) in a different set-up. The master curve is a Gamma distribution of order n around 4 to 5.

We now consider the value of n and why it is insensitive to the external parameters on one hand, and on the other hand determine the value of the average drop size which, by contrast, varies by a factor 3 across the parameter space (figure 12).

5.1. *Ligaments corrugations*

We consider the inelastic collision of two identical jets with diameter d_1, velocity u_1 merging at an angle 2θ (see the Appendix). These jets are intended to model the sheet rim and 2θ is the angle of an indentation cusp (figure 11). The associated Weber number $We_1 = \rho u_1^2 d_1/\sigma$ is *de facto* of order unity, in fact somewhat larger, and in any case smaller than $4(1+\cos\theta)/(\sin\theta)^2$, the value above which the jets form a sheet (Bremond & Villermaux 2006). The collision thus forms a free ligament of mean diameter d and velocity u.

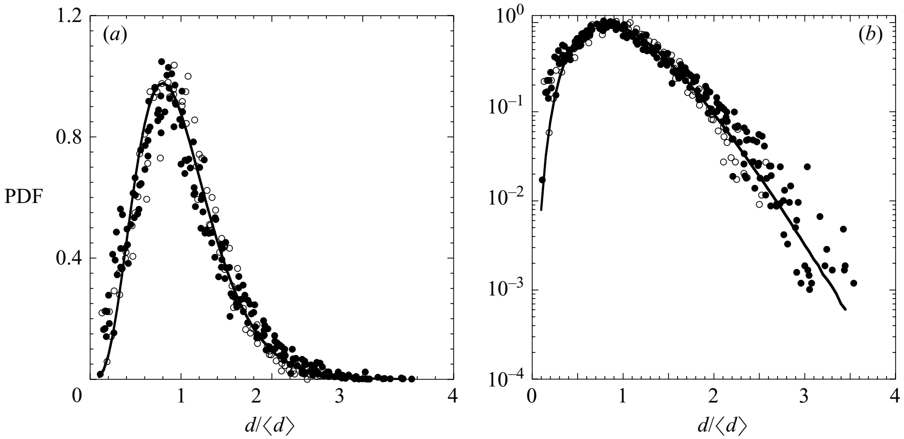

FIGURE 23. (*a*) Probability density functions of the drop size d normalized by the arithmetic mean $\langle d\rangle$ for a number of jet velocities u_j and for several conditions of forcing (●) as well as without forcing (○). The solid curve represents the Gamma function with $n = 5$. (*b*) Semi-logarithmic representation of the size distributions shown in (*a*).

The incoming jets (labelled $i = 1, 2$) are assumed to be corrugated, with amplitude ξ_{11} and ξ_{12} such that $\overline{\xi_{1i}} = 0$ and the $\overline{\xi_{1i}^2}/d_1^2$ are given. The overbar denotes a temporal average i.e. $\overline{(\cdot)} = \lim_{T\to\infty}\int^T(\cdot)\mathrm{d}t/T$. We do not consider, for simplicity, fluctuations in velocity. Neglecting capillary pressure terms because $We_1 > 1$ (see however the Appendix), mass and momentum conservation are written

$$\overline{u_1(d_1+\xi_{11})^2} + \overline{u_1(d_1+\xi_{12})^2} = \overline{u(d+\xi)^2}, \tag{5.2}$$

$$\left(\overline{u_1^2(d_1+\xi_{11})^2} + \overline{u_1^2(d_1+\xi_{12})^2}\right)\cos\theta = \overline{u^2(d+\xi)^2}, \tag{5.3}$$

$$\overline{u_1^2(d_1+\xi_{11})^2} = \overline{u_1^2(d_1+\xi_{12})^2}, \tag{5.4}$$

if the outward ligament is, in the mean, in the median direction ($\theta = 0$). This is so at the condition given by equation (5.4) i.e. $\overline{\xi_{11}^2} = \overline{\xi_{12}^2} \equiv \overline{\xi_1^2}$, giving

$$u = u_1\cos\theta. \tag{5.5}$$

The mean issuing ligament diameter d is, neglecting the contribution $O(\xi^2)$, given by

$$\frac{d}{d_1} = \sqrt{\frac{2}{\cos\theta}}, \tag{5.6}$$

and so

$$\frac{\overline{\xi^2}}{d^2} = \frac{\overline{\xi_1^2}}{d_1^2}. \tag{5.7}$$

Equation (5.7) expresses that the relative roughness of the jets is conserved through the merging process, setting the relative roughness of the issuing ligament. That in turn sets the width of the resulting drop size distribution, when the ligament has broken into disjointed pieces, since it has been argued (Villermaux *et al.* 2004) that the parameter n in equation (5.1) is

$$n = \frac{d^2}{\overline{\xi^2}}. \tag{5.8}$$

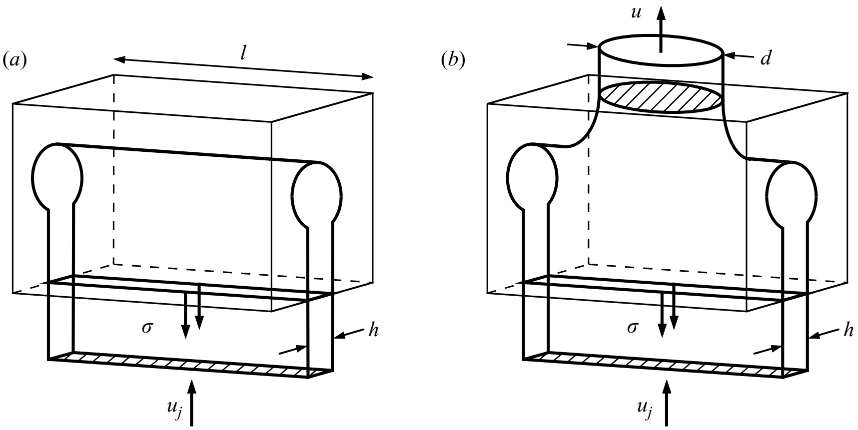

FIGURE 24. Schematic of momentum balance: (*a*) the closed, Culick limit; (*b*) the opened rim, emitting a ligament.

A value of n around 4 to 5 (figure 23) thus reflects a strong corrugation of the initial jets bordering the sheet with an amplitude of the order of the jet diameter ($\sqrt{\overline{\xi_1^2}} \approx d_1/2$). This is a sign that various instabilities affecting the jets have reached their saturation level, independently of the injection parameters (see figure 11 and Huang 1970).

5.2. *Mean drop size*

Once n is known, knowledge of the mean drop size $\langle d \rangle$ is sufficient to represent the entire drop size distribution in the spray. The rim bordering the sheet is the location where the transition to ligaments, mediating drop formation, occurs. Detailed balances are required in order to predict the typical drop size.

5.2.1. *Taylor–Culick's law*

We first recall the standard result by Taylor (1959*b*) and Culick (1960) which, after attempts by Dupré (1868), and Rayleigh (1891), solved the problem of the receding, straight and closed rim attached to a plane sheet. We denote as p_1 and u_j the pressure and velocity in the incoming sheet, h its thickness as it hits the rim, and ℓ the rim length over which momentum balance is written (figure 24*a*)

$$p_1 h\ell + \rho u_j^2 h\ell = 2\sigma\ell. \tag{5.9}$$

If p_1 is taken equal to 0 for a flat sheet, then we obtain the well-known result

$$u_j^2 = \frac{2\sigma}{\rho h}. \tag{5.10}$$

5.2.2. *A generalized Taylor–Culick's law*

We now generalize the above construction to the case of an opened rim, no longer closed at its rear edge, but allowing a ligament to be emitted (figure 24*b*). We first assume that the ligament is emitted in the plane of the sheet and disregard rim curvature in the sheet plane (which may have an impact at small Weber number see Bush & Aristoff 2003). We also neglect the momentum carried by the waves when the sheet is undulating, since $a_0\omega_0/u_j \ll 1$. Denoting as u and p the ligament velocity and internal pressure and d its diameter, we have

$$p_1 h\ell + \rho u_j\, u_j h\ell - 2\sigma\ell = \rho u\, u\frac{\pi d^2}{4} - \pi d\sigma + p\frac{\pi d^2}{4}, \tag{5.11}$$

$$u_j h\ell = u\frac{\pi d^2}{4}, \tag{5.12}$$

for momentum and mass conservation. We check that the standard Culick's law is recovered when the rim is made impermeable, i.e. when $u = d = 0$. Setting $p_1 = 0$ as before for a flat sheet, and $p = 2\sigma/d$ according to Laplace's law for an elongated thread, we have

$$\rho u_j(u_j - u) = \frac{2\sigma}{h} - \frac{\pi d\sigma}{2h\ell} \tag{5.13}$$

or equivalently

$$1 - \frac{u}{u_j} = \frac{2\sigma}{\rho u_j^2 h}\left(1 - \frac{\pi d}{4\ell}\right) \tag{5.14}$$

which generalizes Culick's law to the open case. Adapting this result to Savart's radially expanding sheet for which $h = d_j^2/8R$ and where we have set $R_0 = d_j We/16$ (§ 2), we have

$$1 - \frac{u}{u_j} = \frac{R}{R_0}\left(1 - \frac{\pi d}{4\ell}\right). \tag{5.15}$$

Now ℓ is, according to the balance in equation (5.11), the portion of rim length from which a single ligament is emitted. It is at this stage unknown, and can be fixed by any external effect. We have mentioned that the number of cusps bordering the sheet is apparently constant as can be seen from the top views of the sheet shown in figures 10(*b*), 10(*c*) and 10(*d*). From the analysis of the secondary instability in § 4.1, this fact is consistent with the property of the Rayleigh–Taylor instability in the small thickness limit: there is, in the limit $k_c h \ll 1$, essentially no mode selection in the range of unstable modes, because the dispersion equation there is flat, with a plateau for $0 < k < k_c$; all transverse wavelengths are amplified at the same rate ω_t, and those setting the indentation width at the rim are likely to be caused by minute imperfections of the injector and/or the impact cylinder. Let n_c be the number of cusps, then obviously $\ell = 2\pi R/n_c$ so that

$$1 - \frac{u}{u_j} = \frac{R}{R_0} - \frac{n_c}{8}\frac{d}{R_0}. \tag{5.16}$$

Experiments indicate that $d/d_j = O(1)$ and since $R_0/d_j \sim We \gg 1$, approximately

$$\frac{u}{u_j} \approx 1 - \frac{R}{R_0}. \tag{5.17}$$

Global mass conservation expressing that all the n_c ligaments carry the injected flow rate gives

$$\left(\frac{d_j}{d}\right)^2 = n_c\frac{u}{u_j}. \tag{5.18}$$

Using equations (5.17) and (5.18), one finally anticipates that the ligament diameter will be

$$\frac{d_j}{d} = \sqrt{n_c\left(1 - \frac{R}{R_0}\right)}. \tag{5.19}$$

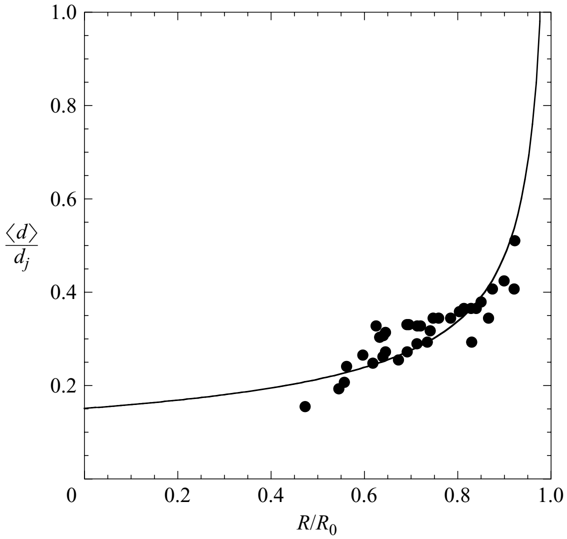

FIGURE 25. Mean drops size $\langle d \rangle$ normalized by the jet diameter d_j as a function of the relative sheet radius R/R_0; the solid curve is the estimate given by equation (5.19) for a fixed number of cusps n_c adjusted to 44.

By analogy with the breakup of a smooth liquid thread, we further assume that the mean drop diameter $\langle d \rangle$ is proportional to the liquid thread diameter d given above (there might, however, be deviations from this rule for strongly corrugated ligaments of finite volume, see Villermaux *et al.* (2004) and an illustration in Marmottant & Villermaux (2004*b*)). The mean drop size, measured when the sheet is forced, is plotted in figure 25 versus the experimental value of R/R_0 superimposed with relationship (5.19) with $\langle d \rangle \equiv d$ for a fixed number of cusps adjusted to $n_c = 44$ which, despite the spreading and the narrow range, correlates the data well.

5.2.3. *The issue of dissipation*

We have written the balances in § 5.2.2 assuming that mass and momentum are ejected the ligament both in the same direction, aligned with the incoming flow in the sheet. That situation implies that some energy is dissipated during the passage through the rim. Disregarding surface energy contributions (weak as long as $We \gg 1$), the loss of mechanical energy q is

$$q = \frac{1}{2}\rho(u_j^2 - u^2) = \frac{1}{2}\rho u_j^2 \frac{R}{R_0}\left(2 - \frac{R}{R_0}\right) \qquad (5.20)$$

if use is made of equation (5.17) for the link between u and u_j, a result somewhat analogous to that of Carnot for energy loss in pipes of varying section.

One may imagine an alternative scenario, where the Culick equilibrium is still satisfied (or its generalized version in equation (5.14)), but where no dissipation occurs. De Gennes (1996) has suggested, in the context of soap films, that the drops could be ejected at an angle with respect to the sheet plane. Translated into our situation, the ligaments would leave the rim with a velocity component $u_\perp$ perpendicular to the sheet plane (in a symmetrical fashion), and a longitudinal component $u_\parallel$ satisfying the generalized Culick equilibrium such that $u_\parallel/u_j = 1 - R/R_0$ according to equation (5.17). No dissipation occurs when $u_\parallel^2+u_\perp^2=u_j^2$, that is for

$$u_\perp = u_j\sqrt{\frac{R}{R_0}\left(2-\frac{R}{R_0}\right)}. \tag{5.21}$$

According to this view, when $R/R_0\rightarrow 1$ (in the smooth regime for instance), when $u_\parallel\rightarrow 0$, that is all the incident momentum is absorbed in the sheet plane, the ligaments should leave the rim with a perpendicular velocity $u_\perp$ of the order of the injection velocity u_j, in the same manner as the initial jet was redistributed radially when impacting the solid cylinder. This is clearly not what occurs, as can be seen for instance on figure 3 where the drops, once formed, essentially fall by their own weight, and leave the rim with no appreciable velocity. The rim does dissipate a large amount of mechanical energy, as already noted by Taylor (1959*b*), and later quantified in Clanet & Villermaux (2002): about 90 % of the incident kinetic energy is dissipated in the rearrangements accompanying the sheet–ligament–drops transition in the smooth regime. This fraction decays as R/R_0 diminishes, but the ligaments and issuing drops are still essentially released in the sheet plane.

This discussion underlines that we have no *ab initio* principle to decide what fraction of the initially available energy is dissipated, or converted into another form – surface energy for instance – in any given particular situation (see also the Appendix). The energy budget is a consequence of the conservation principles for mass and momentum. But when those cannot be expressed unambiguously, as in the present case, a degree of freedom is left for heuristic speculations.

5.3. *Natural flapping*

We finally translate the results obtained in § 4.1 to the ‘natural’ situation when the sheet is no longer artificially vibrated, but when the undulations come from the Squire, shear instability (§ 3). In that case, the most amplified wavenumber has been shown to be given by $\tilde{k}_m=\alpha We/5$ corresponding to a wavelength $\lambda_m\sim\sigma/\rho_a u_j^2$. The pulsation ω_0 in equation (4.9) giving the sheet radius is then $\omega_0\approx k_m u_j(1-(R/R_0)^{1/2})$ as shown in § 3 so that a direct application of equation (4.9) provides, *mutatis mutandis*, the sheet radius R in the form

$$C16^{-3/2}\alpha We^2\left(\frac{R}{R_0}\right)^{3/2}=\ln\left(\frac{d_j}{a_0\alpha We}\right) \tag{5.22}$$

or, written as a function of the initial jet diameter d_j,

$$\frac{R}{d_j}\sim\alpha^{-2/3}We^{-1/3}\ln\left(\frac{d_j}{a_0\alpha We}\right)^{2/3}, \tag{5.23}$$

where the logarithm is approximately constant for large d_j/a_0, a result already found by Huang (1970) from other arguments. The scaling $R\sim\alpha^{-2/3}We^{-1/3}$ in equation (5.23) reflects the weight of the different quantities in the gain of the primary instability given by equation (3.10). It is expected to hold as soon as at least one unstable primary shear wavelength λ_m fits into the unperturbed radius R_0, a condition which occurs for

$$We\gtrsim\frac{40}{\sqrt{\alpha}} \tag{5.24}$$

as anticipated in Villermaux & Clanet (2002), giving $We\gtrsim 1000$ for the couple water/air at normal pressure. This condition equivalently expresses that the transit

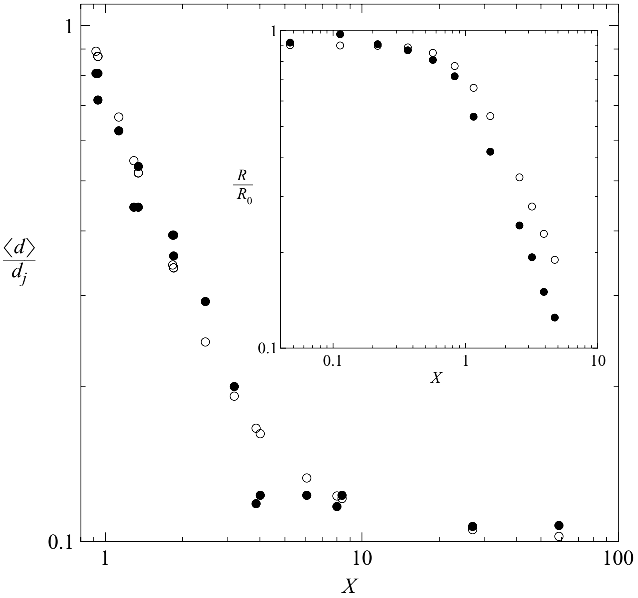

FIGURE 26. Mean drop size in the naturally flapping regime versus reduced Weber $X = (\alpha We^2/40^2)^{2/3}$: ●, data from Villermaux & Clanet (2002); ○, value expected from equation (5.19) making use of equation (5.25). Inset: Corresponding sheet radius: ●, data from Villermaux & Clanet (2002); ○, expected value from equation (5.25) with $\zeta = 3$.

time over a primary undulation wavelength $T \sim \lambda_m/\Delta u \approx \lambda_m/u_j$ is shorter than the global transit time R/u_j with R given by equation (5.23). The second, Rayleigh–Taylor instability time scale should also be equal to T according to the criterion of equation (4.6) for breakup of the sheet to occur. However, the growth of the primary undulations is the slowest process, and its development therefore governs the global extent of the sheet.

An overall parameterization of the sheet radius (figure 26) is for instance as follows:

$$\frac{R}{R_0} = \frac{1}{(1 + X^{\zeta})^{1/\zeta}} \qquad \text{with} \qquad X = \left(\frac{\alpha We^2}{40^2}\right)^{2/3}, \tag{5.25}$$

bridging the smooth (for which $R/R_0 \approx 1$) and flapping (for which $R/R_0 \sim \alpha^{-2/3} We^{-4/3}$) regimes. The stiffness exponent in the fit of equation (5.25) is $\zeta = 3$ (see figure 26).

The mean drop size in this flapping regime is now evaluated along the same lines as those of §5.2.2: we assume a constant number of cusps, and use equation (5.19). From figure 26, it is seen that $\langle d\rangle/d_j$ varies, from the onset of flapping at $X = 1$ to the utimate saturation for $X \gg 1$, by a factor 10 approximately. This indicates, from equation (5.19), that the effective number of cusps in that case (the data are from Villermaux & Clanet (2002), for a different set-up) is $10 = \sqrt{n_c}$, from $n_c = 100$. Inserting the value of R/R_0 from equation (5.25) into the anticipated value for the mean drop diameter in equation (5.19), figure 26 shows that both the rapid decrease of $\langle d\rangle$ with X (or We), and its saturation are accounted for well.

6. Conclusion

This paper has attempted to give a comprehensive description of the atomization of undulating, radially expanding liquid sheets formed by the impact of a liquid jet with a solid obstacle. The undulation was either artificially triggered by the oscillation of the impact point, or the result of a natural shear instability with the ambient medium.

From the observations made in this study, several lessons can be drawn:

The propagation of the undulation waves along the sheet, may they be marginally stable or unstable, is described well by linear theory. The stability limits, the dynamics of the wave amplitude and group velocity are satisfactorily predicted by the standard Squire dispersion relation.

A subtle secondary instability, again completely understood on a linear basis, is responsible for thickness modulations of the sheet. The mechanism, 'the wavy corridor', relies on transient accelerations imparted to the sheet involving a centrifugal instability of a Rayleigh–Taylor type, modified by the finiteness of the sheet thickness. It explains the emergence of azimuthal thickness modulations, and may be a precursor of the longitudinal folds close to the sheet edge, terminated by ligaments. This instability, coupled with the undulation dynamics, provides the relevant time scale for understanding the radial location at which the sheet disintegrates.

The sheet–drop transition is mediated by the formation of ligaments, whose formation conditions characterize completely the drop size distribution in the resulting spray. This transition is highly dissipative, although the amount of dissipated energy is not solely responsible for the broadness of the size distribution, which is mainly caused by the corrugated nature of the rim bordering the sheet as a result of various instabilities.

Of critical importance to understanding the mean drop size is the number of cusps, the locations of ligament emission at the sheet edge. It has been argued that this number is roughly constant, independent of the sheet size, and essentially the result of imperfections of the injection conditions, amplified by the secondary, broadband centrifugal instability. This is consistent with the experimental observations, but though the origin of these cusps seems to be related to the thickness modulations of the sheet, their shape and dynamics remain obscure. They are very likely to be the saturated state of the straight receding rim instability, a yet unsolved – but fundamental – issue of free liquid sheet physics.

This work was supported by CNES under contract 02-0485-00.

Appendix. Roughness creation from jet merging

Consider the inelastic collision of two identical jets with diameter d_1, velocity u_1 merging at an angle 2θ. As explained in § 5.1, these jets are intended to model the sheet rim and 2θ is the angle of an indentation cusp. The jet Weber number $We_1 = \rho u_1^2 d_1/\sigma$ is larger than unity, albeit moderate, say typically 5 to 10 (figure 27). We provide here a slightly more general discussion of the conservation laws in this system, and we show how, starting with initially smooth jets, the rate of surface energy destruction in the merging process explains the corrugation amplitude of the resulting jet, and consequently the width of the drop size distribution thus formed.

We take the jets as initially smooth, and denote as u and p the resulting ligament velocity and internal pressure, and d its diameter (figure 27). Momentum and mass conservation are written

$$\rho u_1 \cos\theta \, 2u_1 d_1^2 - \rho u \, u d^2 = (p - p_1) d^2, \tag{A 1}$$

$$2u_1 d_1^2 = u d^2. \tag{A 2}$$

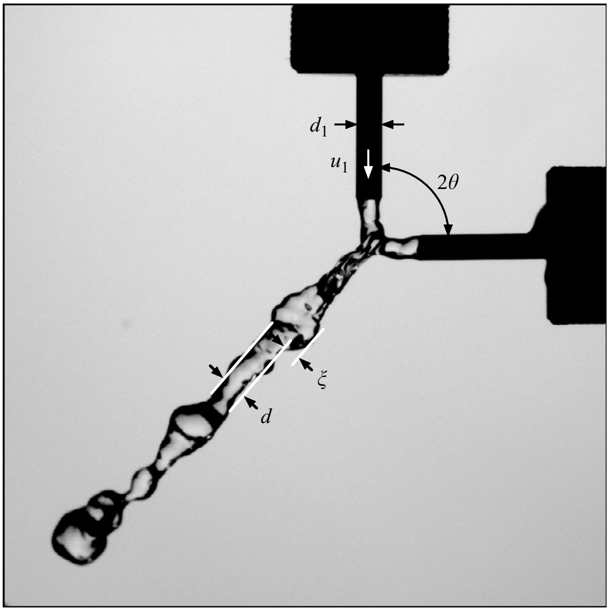

FIGURE 27. Impact at an angle and merging of two liquid jets with small Weber number ($We = 5$).

Surface tension does not enter explicitly in this balance, only through the internal pressures $p_1 = 2d_1/\sigma$ and $p = 2d/\sigma$. The pressure difference before and after merging is given according to the above system by

$$p_1 - p = \rho u(u - u_\parallel) \qquad \text{with} \qquad u_\parallel = u_1 \cos\theta. \tag{A 3}$$

On a pressure scale given by the incident kinetic pressure ρu_1^2, the pressure difference $p_1 - p = 2/\sigma(1/d_1 - 1/d)$ is of order We_1^{-1}. The velocity of the resulting jet u is thus

$$u \approx u_\parallel = u_1 \cos\theta \tag{A 4}$$

at the precision $We_1^{-1} = O(1/10)$, typically so that $d/d_1 \approx \sqrt{2/\cos\theta}$. However, the loss of energy q during the collision

$$q = \frac{1}{2}\rho u_1^2(1 - \cos^2\theta) + \frac{2\sigma}{d_1}\left(1 - \frac{d_1}{d}\right) \tag{A 5}$$

is finite, and dominated by the surface energy term, corresponding to a destruction of surface area in the collision,

$$q = \frac{2\sigma}{d_1}\left(1 - \frac{1}{\sqrt{2}}\right) + O(\theta^2). \tag{A 6}$$

It is immediately clear that when two cylinders of diameter d_1 and height $\ell_1 = u_1\Delta t$ merge to give a unique cylinder of diameter $d = d_1\sqrt{2/\cos\theta}$ and height $\ell = u\Delta t$ of identical volume, the net mean surface destruction per unit volume is given by q/σ (figure 28).

As mentioned in § 5.2.3, we have no *ab initio* principle to decide how this energy will be dissipated. Irregular motions in the bulk of the resulting jet will ultimately

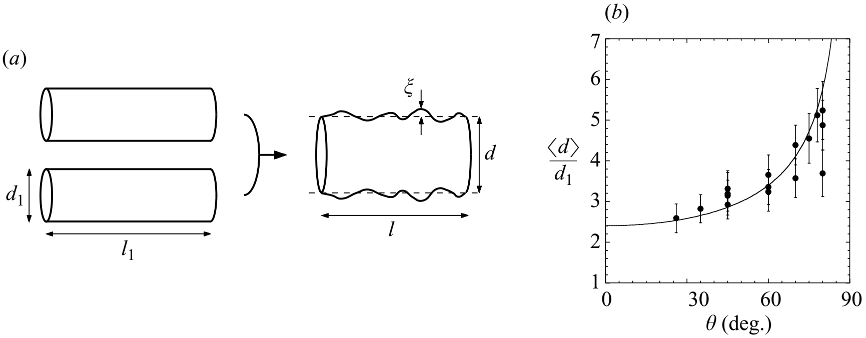

FIGURE 28. (*a*) Schematic of jet merging, and surface roughness generation. Corrugations expanded in Fourier modes: $\xi = \sum_k \epsilon_k \cos(kx)$. (*b*) Dependence of the average drop size from the destabilization of the resulting jet on the impact angle. Solid line is $\langle d\rangle/d_1 = \sqrt{2/\cos\theta}$.

decay by viscous friction, briefly exciting capillary waves at its surface. We may, without precise proof, invoke a kind of equipartition between agitation and surface energy by analogy with the thermal equilibrium limit (Safran 2003), the situation here being further complicated by the fact that the cylindrical jet geometry is not in equilibrium since it sustains a capillary-driven instability. The change of surface area ΔS, at constant volume, of a cylinder whose radius $d/2$ is corrugated by an axisymmetric harmonic perturbation of wavenumber k and amplitude ϵ_k is (Plateau 1873)

$$\frac{\Delta S}{\pi d \ell} = \frac{\epsilon_k^2}{d^2}\left\{\left(\frac{kd}{2}\right)^2 - 1\right\}. \tag{A 7}$$

We attribute the amount of energy ultimately dissipated to the (transient) excess of surface energy (implying *de facto* that $k > 2/d$)

$$\sigma \Delta S \sim q \frac{\pi d^2}{4} \ell \tag{A 8}$$

with an unknown pre-factor, presumably of order unity. This provides the relative amplitude of the corrugations thus formed:

$$\frac{\epsilon_k^2}{d^2} = \frac{1}{2}\frac{\sqrt{2}-1}{\left(\frac{1}{2}kd\right)^2 - 1}. \tag{A 9}$$

In the confluence region, the resulting jet is obviously essentially excited at a scale given by the size of the incoming jets d_1. Setting therefore $k = 2\pi/d_1$, and remembering that the width of the (Gamma) drop size distribution coming from the breakup of the resulting jet will be set by the corresponding order $n = d^2/\epsilon_k^2$, one anticipates that

$$n = \frac{4\pi^2 - 2}{\sqrt{2}-1} \approx 90. \tag{A 10}$$

Figure 29 indeed shows that when two nearly (but not strictly) smooth jets merge, they give rise to drop distributions essentially independent of the merging angle, fitted well by Gamma distributions with an order ($n = 70$) somewhat smaller than the expected one, this latter difference being a sign of the residual fluctuations in the incoming jets (see figure 29*a*, *b* and § 5.1). This merging process generates, however,

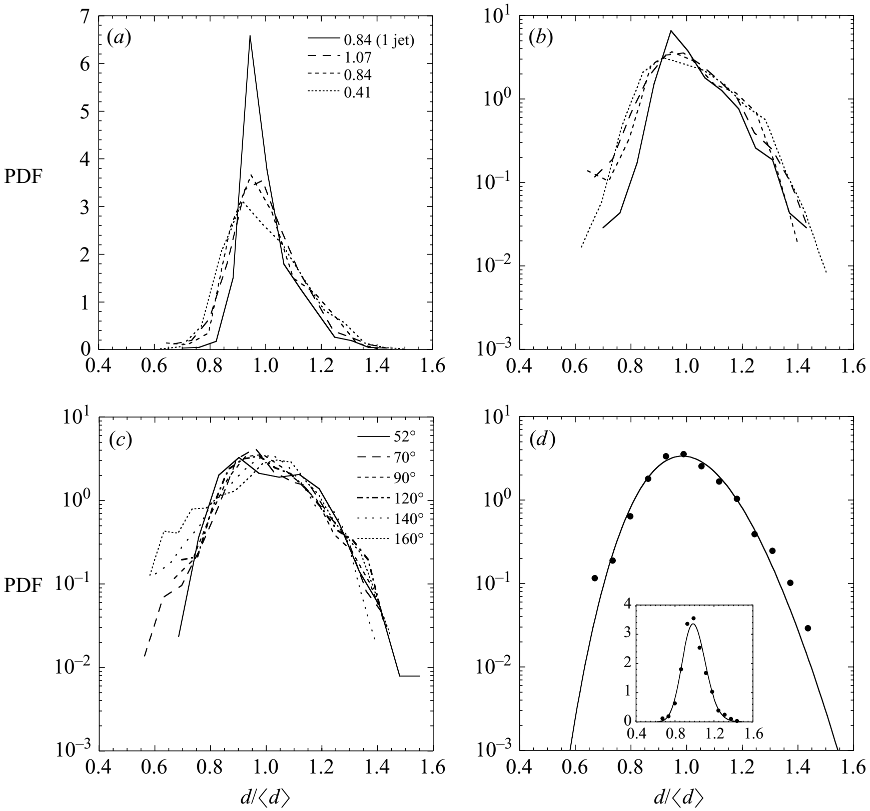

FIGURE 29. Probability density functions (p.d.f.) of the drop size d normalized by the arithmetic mean $\langle d\rangle$. (*a*) Two jets at an angle of 90° and three different diameters d_j. For comparison, the pdf for a single jet is also shown. (*b*) Same as (*a*) in log–lin units. (*c*) An impact angle 2θ varying from 52° to 160° with two identical jets of 1.07 mm. (*d*) Two jets with $d_j = 1.07$ mm, $\alpha = 90°$ superimposed with a Gamma fit with $n = 70$.

weak fluctuation levels, having no correspondence with those attained by the sheet rim destabilization (§ 5.1), those which are responsible for the broadness of the drop size distribution of the sheet breakup.

REFERENCES

ASARE, H. R., TAKAHASHI, R. K. & HOFFMAN, M. A. 1981 Liquid sheet jet experiments: comparison with linear theory. *Trans. ASME: J. Fluids Engng* **103**, 395–604.

BAYVEL, L. & ORZECHOWSKI, Z. 1993 *Liquid atomization*. Taylor & Francis.

BOND, W. N. 1935 The surface tension of a moving water sheet. *Proc. Phys. Soc.* **47**, 549–558.

BREMOND, N. & VILLERMAUX, E. 2005 Bursting thin liquid films. *J. Fluid Mech.* **524**, 121–130.

BREMOND, N. & VILLERMAUX, E. 2006 Atomization by jet impact. *J. Fluid Mech.* **549**, 273–306.

BUSH, J. W. M. & ARISTOFF, J. M. 2003 The influence of surface tension on the circular hydraulic jump. *J. Fluid Mech.* **489**, 229–238.

CHANDRASEKHAR, S. 1961 *Hydrodynamic and Hydromagnetic Stability*. Dover.

CLANET, C. & VILLERMAUX, E. 2002 Life of a smooth liquid sheet. *J. Fluid Mech.* **462**, 307–340.

CULICK, F. E. C. 1960 Comments on a ruptured soap film. *J. Appl. Phys.* **31**, 1128–1129.

DOMBROWSKI, N. & JOHNS, W. R. 1963 The aerodynamics instability and disintegration of viscous liquid sheets. *Chem. Engng Sci.* **18**, 203–214.

Drazin, P. G. & Reid, W. H. 1981 *Hydrodynamic Stability*. Cambridge University Press.

Dupré, A. 1868 Théorie mécanique de la chaleur. *Ann. Chim. Phys.* **11**, 194.

Eggers, J. 1997 Nonlinear dynamics and breakup of free-surface flows. *Rev. Mod. Phys.* **69** (3), 865–929.

Einsenklam, P. 1964 On ligament formation from spinning disks and cups. *Chem. Engng Sci.* **19**, 693–694.

Fraser, R. P., Eisenklam, P., Dombrowski, N. & Hasson, D. 1962 Drop formation from rapidly moving liquid sheet. *AIChE J.* **8**, 672–680.

de Gennes, P. G. 1996 Mechanics of soft interfaces. *Faraday Disc.* **104**, 1–8.

Hagerty, W. W. & Shea, J. F. 1955 A study of the stability of plane fluid sheets. *J. Appl. Mech.* **22**, 509–514.

Heidmann, M. F., Priem, R. J. & Humphrey, J. C. 1957 A study of sprays formed by two impacting jets. *NACA Tech. Note* 3835.

von Helmholtz, H. 1868 On discontinuous movements of fluids. *Phil. Mag.* **36**, 337–346.

Huang, J. C. P. 1970 The break-up of axisymmetric liquid sheets. *J. Fluid Mech.* **43**, 305–319.

James, A. J., Vukasinovic, B., Smith, M. K. & Glezer, A. 2003 Vibration-induced drop atomization and bursting. *J. Fluid Mech.* **476**, 1–28.

Keller, J. B. & Kolodner, I. 1954 Instability of liquid surfaces and the formation of drops. *J. Appl. Phys.* **25**, 918–921.

Kelvin, Lord 1871 Hydrokinetic solutions and observations. *Philo. Mag.* **42**, 362–377.

Kim, I. & Sirignano, W. A. 2000 Three-dimensional wave distortion and disintegration of thin planar liquid sheets. *J. Fluid Mech.* **410**, 147–183.

Lefebvre, A. H. 1989 *Atomization and Sprays*. Hemisphere.

Lin, S. P. 2003 *Breakup of Liquid Sheets and Jets*. Cambridge University Press.

Lozano, A., Garcia-Olivares, A. & Dopazo, C. 1998 The instability growth leading to a liquid sheet break up. *Phys. Fluids* **10**, 2188–2197.

Mansour, A. & Chigier, N. 1990 Disintegration of liquid sheets. *Phys. Fluids* A **2**, 706–719.

Marmottant, P. & Villermaux, E. 2004*a* Fragmentation of stretched liquid ligaments. *Phys. Fluids* **16**, 2732–2741.

Marmottant, P. & Villermaux, E. 2004*b* On spray formation. *J. Fluid Mech.* **498**, 73–112.

Mason, B. J. 1971 *The Physics of Clouds*. Clarendon.

Meier, G. E. A., Klopper, A. & Grabitz, G. 1992 The influence of kinematic waves on jet break down. *Exps. Fluids* **12**, 173–180.

Pandit, A. B. & Davidson, J. F. 1990 Hydrodynamics of the rupture of thin liquid films. *J. Fluid Mech.* **212**, 11–24.

Park, J., Huh, K. Y., Li, X. & Renksizbulut, M. 2004 Experimental investigation on cellular breakup of a planar liquid sheet from an air-blast nozzle. *Phys. Fluids* **16**, 625–632.

Plateau, J. 1873 *Statique Expérimentale et Théorique des Liquides Soumis aux Seules Forces Moléculaires*. Paris, Gauthiers Villars.

Rayleigh, Lord 1879 On the instability of jets. *Proc. Lond. Math. Soc.* **4**, 10.

Rayleigh, Lord 1883 Investigation of the character of the equilibrium of an incompressible heavy fluid of variable density. *Proc. R. Soc. Lond.* **14**, 170–177.

Rayleigh, Lord 1891 Some applications of photography. *Nature* **XLIV**, 249–254.

Safran, S. A. 2003 *Statistical Thermodynamics of Surfaces, Interfaces, and Membranes*. Westview Press.

Savart, F. 1833*a* Mémoire sur la constitution des veines liquides lancées par des orifices circulaires en mince paroi. *Ann. de chim.* **53**, 337–398.

Savart, F. 1833*b* Mémoire sur le choc de deux veines liquides animées de mouvements directement opposés. *Ann. de chim.* **55**, 257–310.

Savart, F. 1833*c* Mémoire sur le choc d'une veine liquide lancée sur un plan circulaire. *Ann. de chim.* **54**, 56–87.

Simmons, H. C. 1977*a* The correlation of drop-size distributions in fuel nozzle sprays. part i : the drop-size/volume-fraction distribution. *J. Engng Power* **7**, 309–314.

Simmons, H. C. 1977*b* The correlation of drop-size distributions in fuel nozzle sprays. part ii : the drop-size/number distribution. *J. Engng Power* **7**, 315–319.

Squire, H. B. 1953 Investigation of the stability of a moving liquid film. *Brit. J. Appl. Phys.* **4**, 167–169.

Taylor, G. I. 1950 The instability of liquid surfaces when accelerated in a direction perpendicular to their plane.i. *Proc. R. Soc. Lond.* A **201**, 192–196.

Taylor, G. I. 1959*a* The dynamics of thin sheets of fluid ii. waves on fluid sheets. *Proc. R. Soc. Lond.* A **253**, 296–312.

Taylor, G. I. 1959*b* The dynamics of thin sheets of fluid iii. disintegration of fluid sheets. *Proc. R. Soc. Lond.* A **253**, 313–321.

Taylor, G. I. 1960 Formation of thin flat sheets of water. *Proc. R. Soc. Lond.* A **259**, 1–17.

Villermaux, E. & Clanet, C. 2002 Life of a flapping liquid sheet. *J. Fluid Mech.* **462**, 341–363.

Villermaux, E., Marmottant, P. & Duplat, J. 2004 Ligament-mediated spray formation. *Phys. Rev. Let.* **92**, 074501.

Weihs, D. 1978 Stability of thin, radially moving liquid sheets. *J. Fluid Mech.* **87**, 289–298.

Worthington, A. M. 1908 *A Study of Splashes*. Longmans, Green & Co.

York, J. L., Stubbs, H. E. & Tek, M. R. 1953 The mechanism of disintegration of liquid sheets. *Trans. ASME*, pp. 1279–1286.